of the refined parameters. They must be reported in as much detail as the diffraction data.

Suggested translations of the English terms uncertainty and standard uncertainty are

Unbestimmtheit, Standardunbestimmtheit in German;

incertitude, incertitude-type in French;

Неопределённость, стандартная неопределённость in Russian.

References

ABRAHAMS, S. C. & MARSH, P. (1987). *Acta Cryst.* A43, 265–269.

ISO (1993). *Guide to the Expression of Uncertainty in Measurement.* International Organization for Standardization (ISO), 1 rue de Varembé, CH-1211 Genève 20, Switzerland.

PRINCE, E. & SPIEGELMAN, C. H. (1992). *International Tables for Crystallography*, Vol. C, pp. 622–624. Dordrecht: Kluwer Academic Publishers.

SCHWARZENBACH, D., ABRAHAMS, S. C., FLACK, H. D., GONSCHOREK, W., HAHN, T., HUML, K., MARSH, R. E., PRINCE, E., ROBERTSON, B. E., ROLLETT, J. S. & WILSON, A. J. C. (1989). *Acta Cryst.* A45, 63–75.

TAYLOR, B. N. & KUYATT, C. E. (1993). *Guidelines for Evaluating and Expressing the Uncertainty of NIST Measurement Results.* NIST Technical Note 1297. National Institute of Standards and Technology, Gaithersburg, MD 20899, USA.

WILSON, A. J. C. (1992). *International Tables for Crystallography*, Vol. C, pp. 583–584. Dordrecht: Kluwer Academic Publishers.

Acta Cryst. (1995). A51, 569–585

Dynamical Theories of Dark-Field Imaging Using Diffusely Scattered Electrons in STEM and TEM

BY Z. L. WANG*

Metallurgy Division, National Institute of Standards and Technology, Building 223, Gaithersburg, MD 20899, USA

(*Received* 26 *September* 1994; *accepted* 13 *February* 1995)

Abstract

Dynamical theories of atomic number sensitive image (or Z-contrast image) formed by thermal diffusely scattered (TDS) electrons are proposed based on first-principles considerations. 'Exact' theories are derived for simulating images obtained either in scanning transmission electron microscopy (STEM) using an annular dark-field detector or in transmission electron microscopy (TEM) using an on-axis objective aperture under hollow-cone beam illumination. The atom thermal vibrations are described using lattice dynamics with consideration of phase correlations. The effects that are comprehensively covered in the theory include: dynamical diffraction of the beam before and after TDS, thickness-dependent beam broadening or channelling, Huang scattering from defect regions, coherence of the thermal diffusely scattered electrons generated from the atomic layers packed within the coherent length, multiphonon and multiple phonon excitations, and the detector geometry. Simplified theories have been derived from this unified approach under various approximations. It has been shown that the incoherent imaging theory is a much simplified case of the practical imaging condition, and can be applied only for qualitative image interpretation. The coherent length in the z direction varies with the change of atomic mass in the column. It is thus possible that the z coherence may disappear for heavy elements. Finally, the theory of Huang scattering in high-angle dark-field TEM imaging has been illustrated, and the theoretically expected results have been observed experimentally.

1. Introduction

Atomic number (or projected mass thickness) sensitive high-angle dark-field (HADF) images of crystalline materials have been performed in transmission electron microscopy (TEM) (Bentley, Alexander & Wang, 1990; Treacy, 1993; Otten, 1991) and scanning transmission electron microscopy (STEM) (Pennycook & Jesson, 1990; Xu, Kirkland, Silcox & Keyse, 1990; Liu & Cowley, 1991). In STEM, the image is formed by collecting high-angle diffusely scattered electrons using a high-angle annular dark-field (HAADF) detector when a small electron probe, of diameter smaller than about 2 Å, is scanned across the specimen. The image is thus called a HAADF-STEM image, or 'Z-contrast' image because of the strong dependence of its contrast on atomic number. Based on the reciprocity theorem (Cowley, 1969), an analogous image can be formed in TEM using an on-axis objective aperture under hollow-cone beam illumination. Z-contrast imaging has attracted great attention because of its potential for providing chemical-sensitive structural information at atomic resolution.

*Correspondence address: School of Materials Science and Engineering, Georgia Institute of Technology, Atlanta, GA 30332-0245, USA.

Determination of crystal structures based on HAADF-STEM images strongly relies on quantitative interpretation of the image contrast. The simplest model assumes that the image contrast is the convoluted result of the electron probe with a specimen-dependent projected scattering power function, so that the image contrast is a map of the projected mass thickness (Pennycook & Jesson, 1990). This is the incoherent imaging theory, which ignores the broadening and dynamical diffraction effects of the electron probe, thus the image contrast is determined by Z^2, independent of specimen thickness, where Z is the atomic number. Studies have been performed to examine the mechanism for forming the Z-contrast image, and the results have shown various features of the imaging technique.

The theory by Spence, Zuo & Lynch (1989) suggests that the interference of high-order Laue-zone (HOLZ) Bragg reflections may be important for the formation of the image. Dynamical simulations by Wang & Cowley (1989) indicate that the characteristics of phase contrast imaging may be retained in the image if the HOLZ reflections are the dominant factor. Dynamical multislice calculations based on the Einstein model and single-phonon-scattering model have shown that thermal diffuse scattering (TDS) is the key contributor for forming the atomic number sensitive image; dynamical diffraction of the electron probe by the specimen easily breaks the Z^2 rule even for specimens thinner than 10 nm (Wang & Cowley, 1990). Further theoretical studies have shown that the contribution made by multiphonon scattering at high angles is comparable to that made by single-phonon scattering (Hall, 1965; Amali & Rez, 1992; Pennycook & Jesson, 1991). Experimental measurements by Hillyard, Loane & Silcox (1993) and Hillyard & Silcox (1993) have shown the strong dependence of the image contrast on specimen thickness, indicating the importance of beam broadening and diffraction effects. Recent studies by Jesson & Pennycook (1993) and Treacy & Gibson (1993) based on kinematical scattering theory have suggested the importance of longitudinal coherence along the beam direction, so that the imaging signal is determined by the sum of scattering amplitudes from the atom layers packed within the coherence length. The coherence comes from the phase coupling of atom vibrations along the beam direction and the detection geometry of the annular dark field (ADF) detector, so that the incoherent imaging model may give an incorrect answer in practice.

HADF-TEM and HAADF-STEM images of dislocations have shown anomalous behavior (Cowley & Huang, 1992; Perovic, Howie & Rossouw, 1993; Wang, 1994). It is surprising that dislocations and stoichiometric grain boundaries show bright contrast in the image, so that the image contrast is not necessarily a map of the local chemical composition. It has been shown that the local lattice distortion is a source for generating diffuse scattering (or Huang scattering) and, more importantly, the final image contrast is determined by the diffracting condition set up for on-axis bright-field imaging (Wang, 1994). In this case, the HADF-TEM image is called the Huang scattering contrast image and is a direct result of the diffuse scattering produced by the static displacements of the crystal atoms owing to the presence of defects, dislocations or lattice relaxation (Wang, 1994). The HADF-STEM technique shares many properties with conventional diffraction contrast imaging. Therefore, a full dynamical calculation is required for image interpretation.

All the studies listed above have shown the various features of high-angle dark-field imaging using diffusely scattered electrons. There is not, however, a dynamical theory that can comprehensively cover all these features in a single approach. It is desired that the dynamical diffraction of the probe, thickness-dependent beam broadening, longitudinal coherence due to phase correlation of atomic vibration, and the Huang scattering effect are introduced in a single theoretical scheme. This paper is thus intended to introduce a theory that is best suited for serving such purposes. With the Schrödinger equation as starting point, an 'exact' dynamical theory based on the original scheme of Fanidis, Van Dyck, Coene & Van Landuyt (1989) is introduced (§2.1) and the theory is given in a form best suited for numerical calculation. Then the simplified models are derived from the theory under various approximations. In §2.2, an approximated multislice theory is given in order to reduce the amount of numerical calculations. In §3, the dynamical theory for atomic number sensitive imaging in TEM is outlined. Finally, the theory of Huang scattering in HADF-TEM imaging is illustrated. The theoretically expected results are compared with the experimental observations.

2. Imaging using diffusely scattered electrons in STEM

The HAADF-STEM image is formed by collecting the high-angle scattered electrons using a ring-shape annular detector in the diffraction plane when the small electron probe is scanned across the crystal lattice (Fig. 1). The electron detector is defined by inner (u_1) and outer (u_2) angular cut-offs, and is called annular dark-field (ADF) detector. The electron probe is scanned over the specimen using deflection coils. In any subsequent deflection plane, a convergent-beam electron diffraction (CBED) pattern of the region of the specimen illuminated by the beam is formed for each scanning position. The signal detected by the ADF detector is displayed on a cathode-ray tube with a scan synchronized with that of the incident beam on the specimen, which is the HAADF-STEM image of the specimen.

The image is produced by high-angle Bragg scattered Huang scattering and thermal diffusely scattered electrons. The contribution made by high-angle Bragg reflections and Huang scattering can be calculated

following conventional dynamical diffraction theory and this image intensity due to elastic scattering I_{els} (Wang & Cowley, 1990) is

$$I_{els} = \int \mathrm{d}\mathbf{u} |\Phi_0(\mathbf{u}, z = d)|^2 D(\mathbf{u}), \quad (1)$$

where $D(\mathbf{u})$ is the detection function of the ADF detector,

$$D(\mathbf{u}) = \begin{cases} 1 & \text{for } u_1 < u < u_2 \\ 0 & \text{otherwise.} \end{cases} \quad (2)$$

$\Phi_0(\mathbf{u}, z = d)$ is the two-dimensional Fourier transform of the electron wave function at the exit face ($z = d$) of the crystal and $\mathbf{u}$ is a two-dimensional reciprocal-space vector. There are several mechanisms for generating high-angle scattered electrons. The high-order Bragg reflections preserve many characteristics of the conventional phase contrast, thus their contribution to the Z-contrast image needs to be minimized. The contribution of Huang scattering from the defect regions can be introduced in the multislice calculation by using the modified phase-grating function for each slice, because the static atom displacement due to defects is time independent. For crystals free of defects, the contribution from TDS electrons is the dominant factor. The short-range time-dependent coupling of atom vibrations makes TDS approximately an incoherent scattering process, so that the image contrast can be qualitatively interpreted based on the incoherent imaging theory.

Diffuse scattering at high angles can also be generated by electron–electron scattering (e–e, or Compton scattering) (Eaglesham & Berger, 1994; Bleloch, Castell, Howie & Walsh, 1994). This scattering is a less localized scattering process in comparison to TDS, thus, the e–e scattered electrons mainly contribute to the background in the image. High-resolution structuraly related information is produced by localized TDS and Huang scattering. Therefore, this paper is focused on the images formed by TDS and Huang scattered electrons.

In general, quantitative interpretation of the image is rather complex because of the convoluted results of the various effects, such as beam broadening, dynamical diffraction and phase coupling between atom vibrations. It is thus necessary to consider all the possible components of the scattering process. The theories presented below are mainly focused on the multislice approach because of its convenience for image computation. Dynamical diffuse scattering theories using Green-function and Bloch-wave approaches have been given elsewhere (Wang, 1995; Wang & Li, 1995).

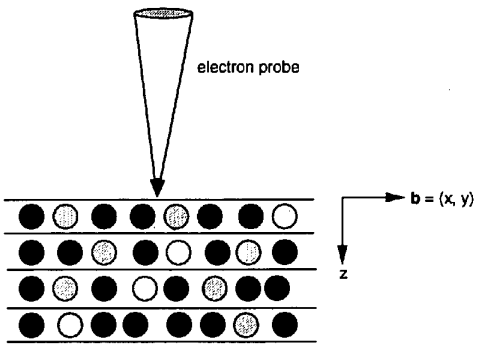

Fig. 1. Schematic diagram showing HAADF-STEM imaging using diffusely scattered electrons.

2.1. *An 'exact' dynamical theory*

The classical theory for treating TDS is based on the 'frozen' lattice model (Hall & Hirsch, 1965), in which all the atoms are seen as if stationary at instantaneous positions by each incident electron, because the vibration period of an atom is about 100 times longer than the interaction time of the electron with the crystal, thus there is almost no atom movement when the electron interacts with the crystal. The experimentally observed image is a time average of the images produced by the crystal lattices of different thermal vibration configurations. The scattering of each instantaneous lattice configuration is approximated as time independent, so that the Schrödinger equation applies (Wang & Bentley, 1991; Wang, 1992).

For crystals containing defects or interfaces, the multislice theory (Cowley & Moodie, 1957) is always applied for simulating the images. The crystal is cut into many parallel slices of equal thickness along the foil-thickness direction, or z-axis direction (Fig. 2), the diffraction of the electron beam by the crystal is calculated consecutively slice-by-slice up to the exit face of the crystal, provided the backscattering is ignored for high-energy electrons. In this approach, the static displacements of atoms near the defect region can be conveniently introduced in the calculation and the only time-dependent process is TDS.

2.1.1. *Basic equations.* For convenience, the real-space multislice theory proposed by Fanidis *et al.* (1989) and Fanidis, Van Dyck & Van Landuyt (1992) is used

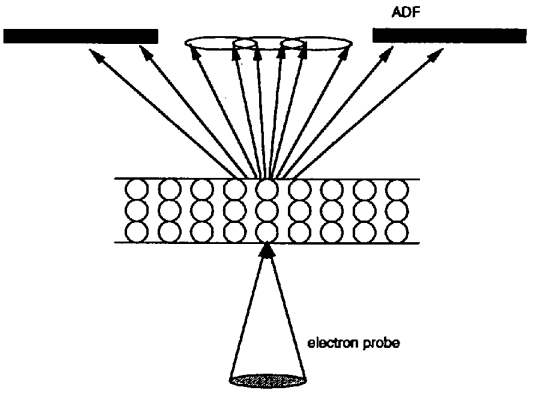

Fig. 2. Schematic diagram showing the multislice approach for calculating electron diffraction in thin crystals.

and further developed here. As will be shown below, this theory not only preserves the full dynamical description of the TDS process but also makes it possible to perform the time averaging of scattering intensity before any numerical calculation. We now start from the Schrödinger equation

$$[\nabla^2 + 4\pi^2(U + K_0^2)]\Psi_0(\mathbf{r}) = 0, \tag{3}$$

where K_0 is the electron wave number and $U = (2m_e e/\hbar^2)\ V$, where V is the crystal potential. V is assumed to be an arbitrary function in accordance with the crystal structure, and can be periodic or non-periodic. For convenience, the time-independent and time-dependent components of the crystal potential are separated so that $U = U_0 + \Delta U(t)$. Under the high-energy approximation, by writing $\Psi_0(\mathbf{r}) = \exp(2\pi i\mathbf{K}_0 \cdot \mathbf{r})\Phi_0(\mathbf{r})$, one can approximate (3) as

$$\partial\Phi_0(\mathbf{r})/\partial z \simeq \zeta[\Xi + 4\pi^2(U_0 + \Delta U)]\Phi_0(\mathbf{r}), \tag{4}$$

where $\zeta = i/4\pi K_{0z} = (iK_0/K_{0z})(\lambda/4\pi)$, where λ is the electron wavelength;

$$\Xi = \nabla_b^2 + 4\pi i\mathbf{K}_{0b} \cdot \nabla_b = \frac{\partial^2}{\partial x^2} + \frac{\partial^2}{\partial y^2} + 4\pi i\left(K_{0x}\frac{\partial}{\partial y} + K_{0y}\frac{\partial}{\partial y}\right) \tag{5}$$

is an operator and $\mathbf{b} = (x, y)$ is the coordinate in the image plane. In order to find the solution of (4), a convenient method is to separate the wave function into two components (Cowley, 1988), one part is the thermally averaged wave function that is independent of the instantaneous vibration status of the crystal lattice and the other part is a small deviation which is strongly affected by the atom vibration,

$$\Phi_0(\mathbf{r}) = \bar{\Phi}_0(\mathbf{r}) + \delta\Phi_0(\mathbf{r}), \tag{6}$$

where $\bar{\Phi}_0(\mathbf{r}) = \langle\Phi_0(\mathbf{r})\rangle$, $\langle\delta\Phi_0(\mathbf{r})\rangle = 0$ and $\langle\ \rangle$ denotes the time average. The boundary conditions are $\bar{\Phi}_0(\mathbf{b}, 0) = \delta_{m0}$ and $\delta\Phi_0(\mathbf{b}, 0) = 0$. Substituting (6) into (4), two coupled equations are obtained (Fanidis *et al.*, 1989, 1992):

$$\frac{\partial}{\partial z}\bar{\Phi}_0 = \zeta(\Xi + 4\pi^2 U_0)\bar{\Phi}_0 + \zeta\langle\Delta U\delta\Phi_0\rangle \tag{7}$$

and

$$\frac{\partial}{\partial z}\delta\Phi_0 \simeq \zeta[(\Xi + 4\pi^2 U_0)\delta\Phi_0 + 4\pi^2\Delta U\bar{\Phi}_0 + 4\pi^2(\Delta U\delta\Phi_0 - \langle\Delta U\delta\Phi_0\rangle)]. \tag{8}$$

We first consider the solution of the time-dependent component. Since the term $(\Delta U\delta\Phi_0 - \langle\Delta U\delta\Phi_0\rangle)$ corresponds to the effects of multiple diffuse scattering, it can be ignored under the first-order approximation, thus,

$$\frac{\partial}{\partial z}\delta\Phi_0 \simeq \zeta[(\Xi + 4\pi^2 U_0)\delta\Phi_0 + 4\pi^2\Delta U\bar{\Phi}_0]. \tag{9}$$

In (9), the ΔU term is the source for generating TDS and $(\Xi + 4\pi^2 U_0)$ is responsible for the elastic re-scattering of the TDS electrons. In dealing with the elastic re-scattering after TDS, it assumes that the crystal potential U_0 is independent of z. This approximation explicitly means that the high-order Laue-zone (HOLZ) reflections have been ignored. Thus, the solution of (9) can be readily written (Fanidis *et al.*, 1989) as

$$\delta\Phi_0(\mathbf{b}, z) \simeq 4\pi^2\zeta\int_0^z dz' O_p(\mathbf{b}, z - z')[\Delta U(\mathbf{b}, z', t)\bar{\Phi}_0(\mathbf{b}, z')], \tag{10}$$

where the operator O_p is defined as

$$O_p(\mathbf{b}, z - z') = \exp[\zeta(\Xi + 4\pi^2 U_0)(z - z')]. \tag{11}$$

The physical meaning of (10) is stated below. The Bragg scattering wave $\bar{\Phi}_0$ is diffusely scattered at z' by ΔU. The subsequent Bragg re-scattering of the diffusely scattered electrons from z' to z is contained in the O_p operator. The multislice calculation of the operator will be given in §2.1.3. The integral on z' is to sum over the TDS waves generated when the electron travels from $z = 0$ to $z = z$. For cases where the electron has lost energy (Yoshioka, 1957), the general form of (10) has been given by Coene & Van Dyck (1990).

2.1.2. *HAADF-STEM image.* The HAADF-STEM images are formed by collecting the high-angle diffusely scatterd electrons in the diffraction plane using a ring-shape annular detector. For a scan position $\mathbf{b}_p$ of the incident electron probe, the intensity distribution in the diffraction plane is the square of the modulus of the Fourier transform of (6),

$$I(\boldsymbol{\tau}) = |\bar{\Phi}_0(\boldsymbol{\tau}, z = d)|^2 + \langle|\delta\Phi_0(\boldsymbol{\tau}, z = d)|^2\rangle, \tag{12}$$

where $\boldsymbol{\tau}$ is a two-dimensional reciprocal-lattice vector in the diffraction plane; the first term includes the Bragg reflections, the second term is TDS and d is the specimen thickness. In general, the deviation potential can be written as a superposition of those for all the atom sites, *i.e.* $\Delta U(\mathbf{r}, t) = \sum_\kappa \Delta U_\kappa(\mathbf{r} - \mathbf{r}_\kappa, t)$, where $\mathbf{r}_\kappa = (\mathbf{b}_\kappa, z_\kappa)$ indicates the position of the atom in the crystal. We now use the solution in (10) to get the angular distribution of TDS electrons,

$$I_{\mathrm{TDS}}(\boldsymbol{\tau}) = \langle|\delta\Phi_0(\boldsymbol{\tau}, z = d)|^2\rangle = |4\pi^2\zeta|^2\left\langle\left|\sum_\kappa \mathbf{F}\left\{\int_0^d dz'\, O_p(\mathbf{b}, d - z') \times [\Delta U_\kappa(\mathbf{b} - \mathbf{b}_\kappa, z' - z_\kappa, t)\bar{\Phi}_0(\mathbf{b}, z')]\right\}\right|^2\right\rangle, \tag{13}$$

where $\mathbf{F}$ denotes the two-dimensional Fourier transform. Equation (13) can be simplified based on the approxima-

tion below. In general, the distribution of the electron wave may not be significantly affected by the scattering of a single-atom layer. Also, the deviation potential ΔU_κ is a localized function with a spatial variation of subatomic dimension. Thus, along the beam direction (z-axis direction), ΔU_κ is the only rapidly varying function within the thickness of a thin slice. Therefore, the dynamical diffraction effect of the atom layer can be ignored, so that the integration on z' is considered to act only on ΔU_κ. Equation (13) is approximated as

$$\begin{aligned} I_{\mathrm{TDS}}(\boldsymbol{\tau}) \simeq |4\pi^2\zeta|^2 \Big\langle \Big| \sum_\kappa \mathbf{F}[O_p(\mathbf{b}, d-z_\kappa) \\ \times \Delta U_\kappa(\mathbf{b}-\mathbf{b}_\kappa, t)\bar{\Phi}_0(\mathbf{b}, z_\kappa)] \Big|^2 \Big\rangle \\ = |4\pi^2\zeta|^2 \sum_\kappa \sum_{\kappa'} \int \mathrm{d}\mathbf{b} \int \mathrm{d}\mathbf{b}' \exp[-2\pi i \boldsymbol{\tau}\cdot(\mathbf{b}-\mathbf{b}')] \\ \times \langle \{O_p(\mathbf{b}, d-z_\kappa)[\Delta U_\kappa(\mathbf{b}-\mathbf{b}_\kappa, t)\bar{\Phi}_0(\mathbf{b}, z_\kappa)]\} \\ \times \{O_p^*(\mathbf{b}', d-z_{\kappa'})[\Delta U_{\kappa'}(\mathbf{b}'-\mathbf{b}_{\kappa'}, t)\bar{\Phi}_0^*(\mathbf{b}', z_{\kappa'})]\}\rangle, \end{aligned} \tag{14}$$

where $\Delta U_\kappa(\mathbf{b}-\mathbf{b}_\kappa, t) = \int \mathrm{d}z' \Delta U_\kappa(\mathbf{b}-\mathbf{b}_\kappa, z'-z_\kappa, t)$ is the projected atomic potential. Since $\mathbf{b}$ and $\mathbf{b}'$ are two distinct variables so that $O_p(\mathbf{b}, d-z_\kappa)$ and $O_p^*(\mathbf{b}', d-z_{\kappa'})$ commute,

$$\begin{aligned} I_{\mathrm{TDS}}(\boldsymbol{\tau}) = |4\pi^2\zeta|^2 \sum_\kappa \sum_{\kappa'} \int \mathrm{d}\mathbf{b} \int \mathrm{d}\mathbf{b}' \exp[-2\pi i \boldsymbol{\tau}\cdot(\mathbf{b}-\mathbf{b}')] \\ \times \{O_p(\mathbf{b}, d-z_\kappa)O_p^*(\mathbf{b}', d-z_{\kappa'})[\langle \Delta U_\kappa(\mathbf{b}-\mathbf{b}_\kappa, t) \\ \times \Delta U_{\kappa'}(\mathbf{b}'-\mathbf{b}_{\kappa'}, t)\rangle \bar{\Phi}_0(\mathbf{b}, z_\kappa)\bar{\Phi}_0^*(\mathbf{b}', z_{\kappa'})]\}. \end{aligned} \tag{15}$$

This equation gives the angular distribution of the TDS electrons in the diffraction pattern. The physical meaning of (15) can be described as follows. The real-space wave function of the elastic scattered wave at depth z is $\bar{\Phi}_0$; the source for generating diffuse scattering at the κth atom site is $[\Delta U_\kappa \bar{\Phi}_0(\mathbf{b}, z_\kappa)]$. The subsequent dynamical diffraction of the diffusely scattered electrons for a thickness $d-z_\kappa$ is included in the O_p operator (see §2.1.3). The time-average term $\langle \Delta U_\kappa \Delta U_{\kappa'}\rangle$ is the result of phase coupling between the atom vibrations, thus determining the coherent scattering behavior of the diffusely scattered electrons generated from atom sites κ and κ'. The beam broadening/channeling effect is contained in $\bar{\Phi}_0(\mathbf{b}, z)$ following the Cowley–Moodie multislice calculation, the modulus squared of which is the probe shape at depth z.

In STEM, if the incident electron probe is centered at $\mathbf{b}_p$ and the elastic wave at depth z is denoted by $\bar{\Phi}_0(\mathbf{b}-\mathbf{b}_p, z)$, the contribution of TDS electrons to the HAADF-STEM image is

$$\begin{aligned} I_{\mathrm{TDS}}(\mathbf{b}_p) = \int \mathrm{d}\boldsymbol{\tau}\, I_{\mathrm{TDS}}(\boldsymbol{\tau})D(\boldsymbol{\tau}) \\ = |4\pi^2\zeta|^2 \sum_\kappa \sum_{\kappa'} \int \mathrm{d}\mathbf{b} \int \mathrm{d}\mathbf{b}' D(\mathbf{b}-\mathbf{b}') \\ \times \{O_p(\mathbf{b}, d-z_\kappa)O_p^*(\mathbf{b}', d-z_{\kappa'}) \\ \times [\langle \Delta U_\kappa(\mathbf{b}-\mathbf{b}_\kappa, t)\Delta U_{\kappa'}(\mathbf{b}'-\mathbf{b}_{\kappa'}, t)\rangle \\ \times \bar{\Phi}_0(\mathbf{b}-\mathbf{b}_p, z_\kappa)\bar{\Phi}_0^*(\mathbf{b}'-\mathbf{b}_p, z_{\kappa'})]]. \end{aligned} \tag{16}$$

This expression has fully incorporated the dynamical scattering of the electrons before and after TDS. No approximation was made in considering the phonon-dispersion relation. The approximations made in deriving (16) are high-energy electron diffraction without back-scattering and first-order thermal diffuse scattering. The calculations of O_p and $\langle \Delta U_\kappa \Delta U_{\kappa'}\rangle$ will be given in §§2.1.3 and 2.1.4, respectively. Equation (16) is the unified imaging theory of HAADF-STEM, which can be applied to calculate the images formed by either low- or high-angle TDS electrons. A few simplified cases of (16) are considered below in order to illustrate its application.

Case a. No dynamical diffraction after TDS, *i.e.* $O_p(\mathbf{b}, d-z_\kappa) = 1$. Thus,

$$\begin{aligned} I_{\mathrm{TDS}}(\mathbf{b}_p) \simeq |4\pi^2\zeta|^2 \sum_\kappa \sum_{\kappa'} \int \mathrm{d}\mathbf{b} \int \mathrm{d}\mathbf{b}' D(\mathbf{b}-\mathbf{b}') \\ \times [\langle \Delta U_\kappa(\mathbf{b}-\mathbf{b}_\kappa, t)\Delta U_{\kappa'}(\mathbf{b}'-\mathbf{b}_{\kappa'}, t)\rangle \\ \times \bar{\Phi}_0(\mathbf{b}-\mathbf{b}_p, z_\kappa)\bar{\Phi}_0^*(\mathbf{b}'-\mathbf{b}_p, z_{\kappa'})]. \end{aligned} \tag{17}$$

It is apparent that the coherence of the HAADF-STEM image is partly determined by the phase coupling between atom vibrations and partly determined by the detection geometry of the ADF detector, as expected from the kinematical scattering theory (Jesson & Pennycook, 1993; Treacy & Gibson, 1993).

Case b. No dynamical diffraction after TDS, and every TDS electron and only TDS electrons are detected, *i.e.* $D(\mathbf{b}-\mathbf{b}') = \delta(\mathbf{b}-\mathbf{b}')$. Thus,

$$\begin{aligned} I_{\mathrm{TDS}}(\mathbf{b}_p) \simeq |4\pi^2\zeta|^2 \sum_\kappa \sum_{\kappa'} \int \mathrm{d}\mathbf{b} [\langle \Delta U_\kappa(\mathbf{b}-\mathbf{b}_\kappa, t) \\ \times \Delta U_{\kappa'}(\mathbf{b}-\mathbf{b}_{\kappa'}, t)\rangle \bar{\Phi}_0(\mathbf{b}-\mathbf{b}_p, z_\kappa) \\ \times \bar{\Phi}_0^*(\mathbf{b}-\mathbf{b}_p, z_{\kappa'})]. \end{aligned} \tag{18}$$

The width of ΔU_κ is much smaller than the interatomic distance, thus for the atoms located in the same crystal slice (*i.e.* the same depth z_κ)

$$\langle \Delta U_\kappa(\mathbf{b}-\mathbf{b}_\kappa, t)\Delta U_{\kappa'}(\mathbf{b}-\mathbf{b}_{\kappa'}, t)\rangle \simeq \langle |\Delta U_\kappa(\mathbf{b}-\mathbf{b}_\kappa, t)|^2\rangle \delta_{\kappa\kappa'}. \tag{19}$$

This means that the TDS electrons generated from the atoms located in different atomic columns of the same slice are approximately incoherent (see Fig. 3) (Wang, 1992; Jesson & Pennycook, 1993; Treacy & Gibson, 1993). This transverse incoherency is the result of assuming $D(\mathbf{b}) = \delta(\mathbf{b})$, which is determined by the detection geometry of the ADF detector. The condition under which $D(\mathbf{b}) = \delta(\mathbf{b})$ will be discussed in §2.1.5.

For the atoms constrained within the same column along the beam direction, however, the coherence of the

TDS electrons may be preserved (Fig. 3), but the coherent length is determined by the phonon-dispersion characteristics of the crystal, as will be discussed in §2.1.5. Thus, (18) becomes

$$I_{\mathrm{TDS}}(\mathbf{b}_p) \simeq |4\pi^2\zeta|^2 \sum_{\kappa} \int \mathrm{d}\mathbf{b}\,[\langle|\Delta U_\kappa(\mathbf{b}-\mathbf{b}_\kappa, t)|^2\rangle \times |\bar{\Phi}_0(\mathbf{b}-\mathbf{b}_p, z_\kappa)|^2] + |4\pi^2\zeta|^2 \sum_{\kappa} \sum_{\kappa''\neq\kappa} \int \mathrm{d}\mathbf{b} \times [\langle\Delta U_\kappa(\mathbf{b}-\mathbf{b}_\kappa, t)\Delta U_{\kappa''}(\mathbf{b}-\mathbf{b}_\kappa, t)\rangle \times \bar{\Phi}_0(\mathbf{b}-\mathbf{b}_p, z_\kappa)\bar{\Phi}_0^*(\mathbf{b}-\mathbf{b}_p, z_{\kappa''})], \quad (20)$$

where the sum of κ'' are limited to the atoms located in the same column as the κ atom. The first term in (20) is the result of incoherent scattering and the second term is the coherent scattering from the atoms constrained in the same column but located at different depth z, consistent with the result obtained based on kinematical scattering theory (Jesson & Pennycook, 1993; Treacy & Gibson, 1993). It is important to note that the first term is obtained without making any assumption regarding the thermal vibration model of the crystal. Thus, the phase coupling between the vibrations of the atoms located in the same slice does not affect the image simulation. Therefore, the scattering between the atom columns is incoherent. This conclusion has been reached earlier (Wang, 1992). The numerical calculations of Wang & Cowley (1990) have demonstrated the transverse and longitudinal coherence in HAADF-STEM images.

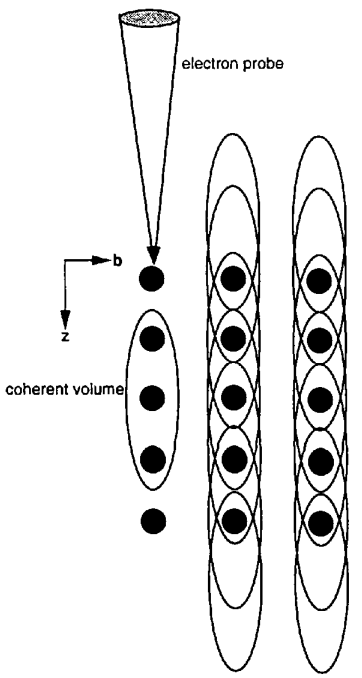

Fig. 3. Transverse incoherence and longitudinal coherence in HAADF-STEM imaging. The coherent volume is approximately indicated by elliptical packets. The incident-beam direction is z.

The coherent lengths can be different for the atomic columns filled with different elements. This may affect the interpretation of image contrast.

Case c. No dynamical diffraction after TDS and no phase coupling between atom vibrations (*i.e.* the Einstein model). Thus,

$$I_{\mathrm{TDS}}(\mathbf{b}_p) \simeq |4\pi^2\zeta|^2 \sum_{\kappa} \int \mathrm{d}\mathbf{b} \int \mathrm{d}\mathbf{b}'\, D(\mathbf{b}-\mathbf{b}') \times [\langle\Delta U_\kappa(\mathbf{b}-\mathbf{b}_\kappa, t)\Delta U_\kappa(\mathbf{b}'-\mathbf{b}_\kappa, t)\rangle \times \bar{\Phi}_0(\mathbf{b}-\mathbf{b}_p, z_\kappa)\bar{\Phi}_0^*(\mathbf{b}'-\mathbf{b}_p, z_\kappa)]. \quad (21)$$

Equation (21) is still unlike the incoherent imaging theory even though the Einstein model has been assumed. Thus, the detection geometry of the ADF detector partly determines the coherence of HAADF-STEM imaging.

Case d. No dynamical diffraction after TDS, no phase coupling between atom vibrations and $D(\mathbf{b}-\mathbf{b}') = \delta(\mathbf{b}-\mathbf{b}')$. Thus,

$$\begin{aligned} I_{\mathrm{TDS}}(\mathbf{b}_p) &= |4\pi^2\zeta|^2 \sum_{\kappa} \int \mathrm{d}\mathbf{b}\,[\langle|\Delta U_\kappa(\mathbf{b}-\mathbf{b}_\kappa, t)|^2\rangle \times |\bar{\Phi}_0(\mathbf{b}-\mathbf{b}_p, z_\kappa)|^2] \\ &= \sum_{n_c} \int \mathrm{d}\mathbf{b}\,|\Gamma(\mathbf{b}, z_{n_c})|^2 |\bar{\Phi}_0(\mathbf{b}-\mathbf{b}_p, z_\kappa)|^2 \\ &= \sum_{n_c} |\Gamma(\mathbf{b}_p, z_{n_c})|^2 \otimes |\Phi_0(\mathbf{b}_p, z_{n_c})|^2, \end{aligned} \quad (22a)$$

where the TDS generation function of the n_cth slice is

$$\begin{aligned} \Gamma^2(\mathbf{b}, z_{n_c}) &= |4\pi^2\zeta|^2 \sum_{\alpha} \langle|V_\alpha(\mathbf{b}-\mathbf{b}_\alpha-\mathbf{u}_\alpha) - V_{0\alpha}(\mathbf{b}-\mathbf{b}_\alpha)|^2\rangle \\ &= |4\pi^2\zeta|^2 \sum_{\alpha} [\langle|V_\alpha(\mathbf{b}-\mathbf{b}_\alpha-\mathbf{u}_\alpha)|^2\rangle - |\langle -V_\alpha(\mathbf{b}-\mathbf{b}_\alpha-\mathbf{u}_\alpha)\rangle|^2], \end{aligned} \quad (22b)$$

the sum of α is over all the atoms located in the n_cth slice and $\otimes$ denotes convolution. Equation (22*a*) looks like the incoherent imaging theory, in which the total intensity is an incoherent sum of those from each individual atom. The theory presented by (22) has been applied to simulate HAADF-STEM images (Wang & Cowley, 1990; Konnert & D'Antonio, 1991).

The atomic number sensitive information is contained in the term $\langle|\Delta U_\kappa(\mathbf{b}-\mathbf{b}_\kappa, t)|^2\rangle$, which is a measure of scattering power of each atom column. The incoherent scattering of each column actually maximizes the Z sensitivity and makes it possible to identify the atom columns directly in the image.

Case e. No dynamical diffraction after TDS, no phase coupling between atom vibrations, $D(\mathbf{b}-\mathbf{b}') = \delta(\mathbf{b}-\mathbf{b}')$ and no beam broadening [*i.e.* $\bar{\Phi}_0(\mathbf{b}-\mathbf{b}_p, z_\kappa) = \bar{\Phi}_0(\mathbf{b}-\mathbf{b}_p, 0)$]. Thus,

$$I_{\mathrm{TDS}}(\mathbf{b}_p) = |4\pi^2\zeta|^2 \sum_{\kappa} \int \mathrm{d}\mathbf{b}\,[\langle|\Delta U_\kappa(\mathbf{b}-\mathbf{b}_\kappa, t)|^2\rangle \times |\bar{\Phi}_0(\mathbf{b}-\mathbf{b}_p, 0)|^2]$$

$$= \left[\sum_{n_c} |\Gamma(\mathbf{b}_p, z_{n_c})|^2\right] \otimes |\Phi_0(\mathbf{b}_p, 0)|^2, \quad (23)$$

where the term $[\sum_{n_c} |\Gamma|^2]$ is the projected TDS-generation scattering of the crystal and $|\Phi_0(\mathbf{b}_p, 0)|^2$ is the probe shape. This equation is the result of incoherent imaging theory. It is thus clear that the incoherent imaging model of HAADF-STEM is a very simplified case of the practical situation. It also appears that the condition $D(\mathbf{b} - \mathbf{b}') = \delta(\mathbf{b} - \mathbf{b}')$ is vital for the incoherent imaging model.

2.1.3. *Multislice calculation of the dynamical scattering operator* O_p. The introduction of the operator O_p has greatly simplified our derivation of the final expression. The image simulations require numerical calculations of a function in the form

$$O_p(\mathbf{b}, d - z_\kappa) X(\mathbf{b}, z_\kappa) = \exp\{\zeta[\Xi + 4\pi^2 U_0](d - z_\kappa)\} X(\mathbf{b}, z_\kappa), \quad (24)$$

where $X(\mathbf{b}, z)$ is assumed to be an arbitrary function and the crystal potential U_0 is independent of z (*i.e.* the projection approximation, which holds only for the reflections in the zero-order Laue zone). This calculation is performed using the Cowley–Moodie multislice method. If the crystal is cut into a total of M slices of equal thickness Δz, *i.e.* $d = M\Delta z$, and assume that the κth atom is located in the n_cth slice, so that

$$O_p(\mathbf{b}, d - z_{n_c}) X(\mathbf{b}, z_{n_c}) = \exp\{\zeta[\nabla_b^2 + 4\pi i \mathbf{K}_{0b} \cdot \nabla_b + 4\pi^2 U_0](M - n_c)\Delta z\} X(\mathbf{b}, z_{n_c}). \quad (25)$$

If the slice thickness is sufficiently small so that for each slice the $\zeta\Delta z(\nabla_b^2 + 4\pi i \mathbf{K}_{0b} \cdot \nabla_b)$ operator and the scattering function $4\pi^2 \zeta \Delta z U_0$ approximately commute, because the second-order term is proportional to Δz^2, for the n_cth slice

$$\begin{aligned} &\exp[\zeta\Delta z(\nabla_b^2 + 4\pi i \mathbf{K}_{0b} \cdot \nabla_b + 4\pi^2 U_0)] X(\mathbf{b}, z_{n_c}) \\ &\simeq \exp[\zeta\Delta z(\nabla_b^2 + 4\pi i \mathbf{K}_{0b} \cdot \nabla_b)] \\ &\quad \times \exp(4\pi^2 \zeta \Delta z U_0) X(\mathbf{b}, z_{n_c}) \\ &= \exp[\zeta\Delta z(\nabla_b^2 + 4\pi i \mathbf{K}_{0b} \cdot \nabla_b)][Q_0(\mathbf{b}, z_{n_c}) X(\mathbf{b}, z_{n_c})], \end{aligned} \quad (26)$$

where $Q_0(\mathbf{b}, z_{n_c}) = \exp(4\pi^2 \zeta \Delta z U_0)$ is the phase-grating function of the slice. The approximation leading to (26) has been discussed in detail by Van Dyck (1983). We now consider the following operation on an arbitrary function $f(\mathbf{b})$ with Fourier transform $f(\mathbf{u})$ (Goodman & Moodie, 1974; Van Dyck, 1975, 1985; Wang, 1995).

$$\begin{aligned} &\exp[\zeta\Delta z(\nabla_b^2 + 4\pi i \mathbf{K}_{0b} \cdot \nabla_b)] f(\mathbf{b}) \\ &= \exp[\zeta\Delta z(\nabla_b^2 + 4\pi i \mathbf{K}_{0b} \cdot \nabla_b)] \\ &\quad \times \int \mathbf{du}\, f(\mathbf{u}) \exp(2\pi i \mathbf{u} \cdot \mathbf{b}) \\ &= \int \mathbf{du} f(\mathbf{u}) \left\{ \sum_{m=0} [\zeta\Delta z(\nabla_b^2 + 4\pi i \mathbf{K}_{0b} \cdot \nabla_b)]^m / m! \right\} \\ &\quad \times \exp(2\pi i \mathbf{u} \cdot \mathbf{b}) \\ &= \int \mathbf{du} f(\mathbf{u}) \left\{ \sum_{m=0} [-4\pi^2 \zeta \Delta z(u^2 + 2\pi i \mathbf{K}_{0b} \cdot \mathbf{u})]^m / m! \right\} \\ &\quad \times \exp(2\pi i \mathbf{u} \cdot \mathbf{b}) \\ &= \int \mathbf{du} f(\mathbf{u}) \exp[-4\pi^2 \zeta \Delta z(u^2 + 2\mathbf{K}_{0b} \cdot \mathbf{u})] \\ &\quad \times \exp(2\pi i \mathbf{u} \cdot \mathbf{b}) \\ &= f(\mathbf{b}) \otimes P(\mathbf{b}, \Delta z), \end{aligned} \quad (27)$$

where P is a propagation function,

$$\begin{aligned} P(\mathbf{b}, \Delta z) &= \int \mathbf{du}\{\exp[-\pi i(u^2 + 2\mathbf{K}_{0b} \cdot \mathbf{u})\Delta z\lambda]\} \\ &\quad \times \exp(2\pi i \mathbf{u} \cdot \mathbf{b}) \\ &= (1/i\lambda\Delta z) \exp[\pi i |\mathbf{b} - \mathbf{K}_{0b}\lambda\Delta z|^2 / \lambda\Delta z]. \end{aligned} \quad (28)$$

Thus,

$$\exp[\zeta\Delta z(\nabla_b^2 + 4\pi i \mathbf{K}_{0b} \cdot \nabla_b)] X(\mathbf{b}, z_{n_c}) \simeq [Q_0(\mathbf{b}, z_{n_c}) X(\mathbf{b}, z_{n_c})] \otimes P(\mathbf{b}, \Delta z). \quad (29)$$

It is important to note that the right-hand side of (29) is just the Cowley–Moodie multislice theory. Finally,

$$\begin{aligned} &O_p(\mathbf{b}, d - z_{n_c}) X(\mathbf{b}, z_{n_c}) \\ &= \exp\left\{\zeta\Delta z \sum_{s=n_c}^{M} [(\nabla_b^2 + 4\pi i \mathbf{K}_{0b} \cdot \nabla_b) + 4\pi^2 U_0]\right\} X(\mathbf{b}, z_s) \\ &\simeq \prod_{s=n_c}^{M} \exp\{\zeta\Delta z[(\nabla_b^2 + 4\pi i \mathbf{K}_{0b} \cdot \nabla_b) + 4\pi^2 U_0]\} X(\mathbf{b}, z_s) \\ &\simeq \{Q_0(\mathbf{b}, z_M)\{Q_0(\mathbf{b}, z_{M-1}) \ldots \{[Q_0(\mathbf{b}, z_{n_c}) X(\mathbf{b}, z_{n_c})] \\ &\quad \otimes P_0(\mathbf{b}, \Delta z)\} \ldots\} \otimes P_0(\mathbf{b}, \Delta z)\} P_0(\mathbf{b}, \Delta z). \end{aligned} \quad (30)$$

This is just the multislice calculation of the electron wave $X(\mathbf{b}, z)$ elastically scattered from the n_cth slice to the exit face of the crystal. Thus, the $O_p(\mathbf{b}, d - z_\kappa)$ operator represents the dynamical diffraction of the electron wave from $z = z_\kappa$ to $z = d$. This calculation does not involve any time-dependent quantity. Diffraction effects of the electron probe and thickness-dependent probe broadening are completely covered in the multislice calculation. Since the phase-grating function Q_0 can be chosen to be different for each slice, it is thus possible to introduce any static defects or dislocations in the multislice calculation. Therefore, the Huang scattering is automatically included. For atoms located in the n_cth slice, the total number of slice calculations is $M - n_c$. For the entire crystal, the total number of slice calculations to be performed is $M_t = \sum_{n_c=1}^{M} (M - n_c) = M(M - 1)/2$. For $M = 50$, $M_t = 1225$.

It is important to note that the theory has fully incorporated the phonon-dispersion relations of the crystal and the Einstein model was not assumed. This is an important advantage of the theory. In the dynamical theory proposed above, the amount of calculation is minimized regarding the time average over the TDS process, but the amount of elastic multislice calculation is increased by a factor of $M/2$. Therefore, as far as TDS is concerned, the amounts of calculation cannot be dramatically reduced without making any further approximations.

2.1.4. *Coupling between atomic vibrations and coherence in HAADF-STEM imaging.* Roughly speaking, phonons are the harmonic modes of crystal lattice vibrations. The phase coupling between atom vibrations is an indication of coherence or partial coherence of the thermal diffusely scattered waves generated from the adjacent atom sites. This effect is included in the time average of the thermal deviation potential. Explicitly writing the deviation potential as the difference of instantaneous atom potential (U_κ) with the potential averaged over time ($U_{0\kappa}$), $\Delta U\kappa = U_\kappa - U_{0\kappa}$, where $U_{0\kappa} = \langle U_\kappa \rangle$ (Takagi, 1958), yields

$$\begin{aligned}
&\langle \Delta U(\mathbf{r}', t)\Delta U^*(\mathbf{r}'', t)\rangle \\
&= \sum_\kappa \sum_{\kappa'} \langle \Delta U_\kappa(\mathbf{r}' - \mathbf{r}_\kappa, t)\Delta U^*_{\kappa'}(\mathbf{r}'' - \mathbf{r}_{\kappa'}, t)\rangle \\
&= \sum_\kappa \sum_{\kappa'} [\langle U_\kappa(\mathbf{r}' - \mathbf{r}_\kappa, t)U^*_{\kappa'}(\mathbf{r}'' - \mathbf{r}_{\kappa'}, t)\rangle \\
&\quad - U_{0\kappa}(\mathbf{r}' - \mathbf{r}_\kappa)U^*_{0\kappa'}(\mathbf{r}'' - \mathbf{r}_{0\kappa'})] \\
&= 4m_e^2e^2/\hbar^4 \sum_\kappa \sum_{\kappa'} \int d\boldsymbol{\tau} \int d\boldsymbol{\tau}' f^e_\kappa(\tau) f^{e*}_{\kappa'}(\tau') \\
&\quad \times \exp[2\pi i\boldsymbol{\tau} \cdot (\mathbf{r}' - \mathbf{r}_{0\kappa}) - 2\pi i\boldsymbol{\tau}' \cdot (\mathbf{r}'' - \mathbf{r}_{0\kappa'})] \\
&\quad \times \{\langle \exp[-2\pi i(\boldsymbol{\tau} \cdot \mathbf{u}_\kappa - \boldsymbol{\tau}' \cdot \mathbf{u}_{\kappa'})]\rangle \\
&\quad - \exp[-W_\kappa(\tau) - W_{\kappa'}(\tau')]\} \\
&= 4m_e^2e^2/\hbar^4 \sum_\kappa \sum_{\kappa'} \int d\boldsymbol{\tau} \int d\boldsymbol{\tau}' f^e_\kappa(\tau) f^{e*}_{\kappa'}(\tau') \\
&\quad \times \exp[2\pi i\boldsymbol{\tau} \cdot (\mathbf{r}' - \mathbf{r}_{0\kappa}) - 2\pi i\boldsymbol{\tau}' \cdot (\mathbf{r}'' - \mathbf{r}_{0\kappa'})] \\
&\quad \times \exp[-W_\kappa(\tau) - W_{\kappa'}(\tau')] \\
&\quad \times \{\exp[4\pi^2\langle(\boldsymbol{\tau} \cdot \mathbf{u}_\kappa)(\boldsymbol{\tau}' \cdot \mathbf{u}_{\kappa'})\rangle] - 1\}, \qquad (31)
\end{aligned}$$

where $f^e_\kappa(\tau)$ is the electron scattering factor of the κth atom, $W_\kappa(\tau) = 2\pi^2\langle|\boldsymbol{\tau} \cdot \mathbf{u}_\kappa|^2\rangle$ is the Debye–Waller factor, $\mathbf{r}_\kappa$ and $\mathbf{r}_{0\kappa}$ are the instantaneous and equilibrium positions, respectively, of the atom, and the atom displacement $\mathbf{u}_\kappa = \mathbf{r}_\kappa - \mathbf{r}_{0\kappa}$. Under the harmonic oscillators approximation, the atom displacement due to thermal vibration is written as a superposition of the contributions from all the phonon modes (Born, 1942; see, for example, Brüesch, 1982)

$$\mathbf{u}_\kappa = \sum_q \sum_i A_\kappa(\mathbf{q}, i)\mathbf{e}_{q,i} \cos[\omega_i(\mathbf{q})t - 2\pi\mathbf{q} \cdot \mathbf{r}_{0\kappa} + \theta_{q,i}], \qquad (32a)$$

where

$$A_\kappa(\mathbf{q}, i) = [\hbar(\langle n_s\rangle + 1/2)/N_0M_\kappa\omega_i(\mathbf{q})]^{1/2}, \qquad (32b)$$

N_0 is the number of primitive unit cells, M_κ is the mass of the atom and $\langle n_s\rangle$ is the average number of phonons at temperature T,

$$\langle n_s\rangle = 1/[\exp(\hbar\omega_i/k_BT) - 1], \qquad (32c)$$

$\mathbf{q}$ is the wave vector of the phonon and i stands for the phonon branch. It can easily be shown that

$$\begin{aligned}
\langle(\boldsymbol{\tau} \cdot \mathbf{u}_\kappa)(\boldsymbol{\tau}' \cdot \mathbf{u}_{\kappa'})\rangle &= \sum_q \sum_i A_\kappa(\mathbf{q}, i)A_{\kappa'}(\mathbf{q}, i) \\
&\quad \times (\boldsymbol{\tau} \cdot \mathbf{e}_{q,i})(\boldsymbol{\tau}' \cdot \mathbf{e}_{q,i}) \\
&\quad \times \cos[2\pi\mathbf{q} \cdot (\mathbf{r}_{0\kappa} - \mathbf{r}_{0\kappa'})] \\
&= [\hbar/N_0(M_\kappa M_{\kappa'})^{1/2}] \\
&\quad \times \sum_q \sum_i [(\langle n_s\rangle + 1/2)/\omega_i(\mathbf{q})] \\
&\quad \times (\boldsymbol{\tau} \cdot \mathbf{e}_{q,i})(\boldsymbol{\tau}' \cdot \mathbf{e}_{q,i}) \\
&\quad \times \cos[2\pi\mathbf{q} \cdot (\mathbf{r}_{0\kappa} - \mathbf{r}_{0\kappa'})] \qquad (33a)
\end{aligned}$$

This function usually decreases with increase of the interatomic distance ($\mathbf{r}_{0\kappa} - \mathbf{r}_{0\kappa'}$). As illustrated in (19), only the longitudinal coherence matters to HAADF-STEM, thus the condition of $4\pi^2\langle(\boldsymbol{\tau} \cdot \mathbf{u}_\kappa)(\boldsymbol{\tau}' \cdot \mathbf{u}_{\kappa'})\rangle \simeq 0$ gives the coherent length of thermal diffuse scattering, leading to the 'cigar'-shaped coherence volume as suggested by Treacy & Gibson (1993) (see Fig. 3). Calculation of (33*a*) has been performed by Wang (1995) based on the Debye model and the Warren (1990) approximation,

$$\langle(\boldsymbol{\tau} \cdot \mathbf{u}_\kappa)(\boldsymbol{\tau}' \cdot \mathbf{u}_{\kappa'})\rangle \simeq \bar{a}^2_\kappa(M_\kappa/M_{\kappa'})^{1/2}\boldsymbol{\tau} \cdot \boldsymbol{\tau}' \mathrm{Si}(\Theta_{\kappa\kappa'})/\Theta_{\kappa\kappa'}, \qquad (33b)$$

where $\mathrm{Si}(\Theta) = \int_0^\Theta du \sin u/u$ and $\Theta_{\kappa\kappa'} = 2\pi q_m|\Delta\mathbf{r}_{\kappa\kappa'}|$, q_m is the radius of the first Brillioun zone, $|\Delta\mathbf{r}_{\kappa\kappa'}| = |\mathbf{r}_{0\kappa} - \mathbf{r}_{0\kappa'}|$ is the interatomic distance and $\bar{a}^2_\kappa$ is the mean square atomic vibration amplitude. Two conclusions can be drawn from (33*b*). Since $\mathrm{Si}(\Theta)/\Theta$ drops quickly with increasing interatomic distance, as shown in Fig. 4, the coherent length for low-angle TDS is much shorter than that for high-angle TDS. The coherent length of light elements is larger than that of heavy elements because $\bar{a}^2_\kappa$ decreases with increasing atomic mass. The coherent length varies with the change of atomic mass in the column. It is thus possible that the z coherence may disappear for heavy elements. In general, the longitudinal coherent length is limited to less than four atoms along the z-axis direction (Jesson & Pennycook, 1993).

Equation (31) contains the contributions from single- and multiphonon scattering. The multiple phonon

scattering, however, has been ignored in the first-order scattering theory.

2.1.5. *Detection geometry and coherence in HAADF-STEM imaging.* We now discuss the conditions under which the $D(\mathbf{b})$ function can be approximated as $\delta(\mathbf{b})$. Consider

$$\begin{aligned} D(\mathbf{b}) &= \int \mathrm{d}\mathbf{u} \exp(2\pi i \mathbf{u}\cdot\mathbf{b}) D(\mathbf{u}) \\ &= \int_0^{u_2} \mathrm{d}u \int_0^{2\pi} \mathrm{d}\varphi\, u \cos(2\pi u b \cos\varphi) \\ &\quad - \int_0^{u_1} \mathrm{d}u \int_0^{2\pi} \mathrm{d}\varphi\, u \cos(2\pi u b \cos\varphi) \\ &= (1/b)[u_2 J_1(2\pi u_2 b) - u_1 J_1(2\pi u_1 b)], \end{aligned} \quad (34)$$

where $J_1(x)$ is the first-order Bessel function. The outer cut-off of the ADF detector is usually large in order to detect the large-angle scattered electrons. Thus, the width of the D function is mainly determined by the inner cut-off of the ADF detector. Since the first zero point of $J_1(x)$ occurs at $x = 3.8317$ (Arfken, 1970), the half-width of the D function is given approximately by

$$b_0 \simeq 3.8317/2\pi u_1 \simeq 0.61\lambda/\theta_1. \quad (35)$$

For 100 keV electrons, $2b_0 \simeq 0.9$ Å for $\theta_1 = 50$ mrad and $2b_0 \simeq 0.45$ Å for $\theta_1 = 100$ mrad. Since the width of the atom potential is less than 1 Å, then the width of the D function cannot be represented by a δ function unless the inner detector angle $\theta_1 > 150$ mrad for 100 keV electrons. This means that the incoherent imaging theory is not exact as far as the size of the detector function is concerned.

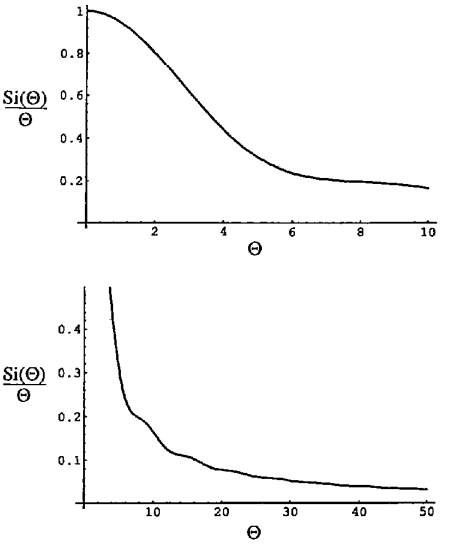

Fig. 4. Plot of the function $\mathrm{Si}(\Theta)/\Theta$.

2.2. *An approximated dynamical theory*

The image calculation can be simplified if the elastic scattering of the electrons after inelastic interaction is ignored. This may be an excellent approximation because the elastic scattering after TDS is approximately limited to the ADF detector angular range, provided it is sufficiently large; thus, the intensity redistribution in the diffraction plane may not affect the signal intensity detected by the ADF detector (Wang & Cowley, 1990). Equation (17) corresponds to such a case, but the high-order TDS is not included. In this case the Cowley–Moodie multislice theory is more convenient to approach the problem.

Based on the frozen lattice model, the electron wave before and after being scattered by a crystal slice of thickness Δz at depth z is correlated (Cowley & Moodie, 1957; Ishizuka, 1982) by

$$\Phi_0(\mathbf{b}, z + \Delta z) = \{\exp[i\sigma' V(\mathbf{b})]\Phi_0(\mathbf{b}, z)\} \otimes P(\mathbf{b}), \quad (36)$$

where $\sigma' = (K_0/K_{0z}\pi e/\lambda E_0)$, where E_0 is the incident electron energy. Since the projected potential of the crystal slice contains the time-dependent perturbation of atom thermal vibration, and it can be written as $V = V_0 + \Delta V$, then (36) is rewritten as

$$\begin{aligned} \Phi_0(\mathbf{b}, z + \Delta z) = \big(&\exp[i\sigma' V_0(\mathbf{b})]\Phi_0(\mathbf{b}, z) \\ &+ \{\exp[i\sigma' V(\mathbf{b})] \\ &- \exp[i\sigma' V_0(\mathbf{b})]\}\Phi_0(\mathbf{b}, z)\big) \otimes P(\mathbf{b}), \end{aligned} \quad (37)$$

where the first term is Bragg scattering and the second term is TDS generated from the crystal slice and can be expressed as

$$\Delta\Phi(\mathbf{b}, z) = i\Gamma(\mathbf{b}, z)\Phi_0(\mathbf{b}, z), \quad (38)$$

where

$$\Gamma(\mathbf{b}, z) = -i\{\exp[i\sigma' V(\mathbf{b})] - \exp[i\sigma' V_0(\mathbf{b})]\}. \quad (39)$$

If the subsequent diffraction of the diffusely scattered electrons is ignored, the intensity detected by the ADF detector may be approximately written as

$$\begin{aligned} I_{\mathrm{TDS}}(\mathbf{b}_p) &= \int \mathrm{d}\mathbf{u} \left\langle \left| \sum_{n_c} \Delta\Phi(\mathbf{u}, z_{n_c}) \right|^2 \right\rangle D(\mathbf{u}) \\ &= \int \mathrm{d}\mathbf{u} \left\langle \left| \sum_{n_c} \Gamma(\mathbf{u}, z_{n_c}) \otimes \Phi_0(\mathbf{u}, z_{n_c}) \right|^2 \right\rangle D(\mathbf{u}) \\ &= \sum_{n_c}\sum_{m_c} \int \mathrm{d}\mathbf{u} \langle [\Gamma(\mathbf{u}, z_{n_c}) \otimes \Phi_0(\mathbf{u}, z_{n_c})] \\ &\quad \times [\Gamma^*(\mathbf{u}, z_{m_c}) \otimes \Phi_0^*(\mathbf{u}, z_{m_c})] \rangle D(\mathbf{u}). \end{aligned} \quad (40)$$

Using the Fourier transforms of Γ and Φ_0, the intensity detected by the ADF detector when the probe is scanned

to $\mathbf{b}_p$ is

$$I_{\mathrm{TDS}}(\mathbf{b}_p) = \sum_{n_c}\sum_{m_c}\int d\mathbf{b}\int d\mathbf{b}'\,\langle\Gamma(\mathbf{b}', z_{n_c})\Gamma^*(\mathbf{b}, z_{m_c})\rangle \times \Phi_0(\mathbf{b}' - \mathbf{b}_p, z_{n_c})\Phi_0^*(\mathbf{b} - \mathbf{b}_p, z_{m_c})D(\mathbf{b} - \mathbf{b}'). \tag{41}$$

Equation (41) has included the contributions of multiphonon and multiple phonon scattering. In general, the time average can be evaluated before any numerical calculation,

$$\begin{aligned}
&\langle\Gamma(\mathbf{b}', z')\Gamma^*(\mathbf{b}, z)\rangle \\
&\quad= \langle\{\exp[i\sigma' V(\mathbf{b}', z')] - \exp[i\sigma' V_0(\mathbf{b}', z')]\} \\
&\qquad\times \{\exp[-i\sigma' V(\mathbf{b}, z)] - \exp[-i\sigma' V_0(\mathbf{b}, z)]\}\rangle \\
&\quad= \exp\{i\sigma'[V_0(\mathbf{b}', z') - V_0(\mathbf{b}, z)]\} \\
&\qquad\times \langle\{\exp[i\sigma'\Delta V(\mathbf{b}', z')] - 1\} \\
&\qquad\times \{\exp[-i\sigma'\Delta V(\mathbf{b}, z)] - 1\}\rangle \\
&\quad= \exp\{i\sigma'[V_0(\mathbf{b}', z') - V_0(\mathbf{b}, z)]\}\big(\langle\exp\{i\sigma'[\Delta V(\mathbf{b}', z') \\
&\qquad- \Delta V(\mathbf{b}, z)]\}\rangle - \langle\exp[i\sigma'\Delta V(\mathbf{b}', z')]\rangle \\
&\qquad- \langle\exp[-i\sigma'\Delta V(\mathbf{b}, z)]\rangle + 1\big) \\
&\quad\simeq \exp\{i\sigma'[V_0(\mathbf{b}', z') - V_0(\mathbf{b}, z)]\} \\
&\qquad\times \big(\exp\{-(\sigma'^2/2)[\langle|\Delta V(\mathbf{b}', z')|^2\rangle \\
&\qquad+ \langle|\Delta V(\mathbf{b}, z)|^2\rangle - 2\langle\Delta V(\mathbf{b}', z')\Delta V(\mathbf{b}, z)\rangle]\} \\
&\qquad- \exp[-(\sigma'^2/2)\langle|\Delta V(\mathbf{b}', z')|^2\rangle] \\
&\qquad- \exp[-(\sigma'^2/2)\langle|\Delta V(\mathbf{b}, z)|^2\rangle] + 1\big).
\end{aligned} \tag{42}$$

The relation $\langle\exp[i\sigma'\Delta V]\rangle \simeq \exp[-(\sigma'^2/2)\langle|\Delta V|^2\rangle]$, provided $\langle\Delta V\rangle = 0$, was used in (42). The time average of the modulus crystal potential can be easily performed by expressing the atom potential as the Fourier transform of the atomic scattering factor, and the results are

$$\begin{aligned}
\langle[\Delta V(\mathbf{b}, z)]^2\rangle &\simeq \sum_\kappa[\langle|V_k(\mathbf{b} - \mathbf{b}_\kappa, z)|^2\rangle - V_{0k}^2(\mathbf{b} - \mathbf{b}_\kappa, z)] \\
&\simeq \sum_\kappa\int d\mathbf{u}\int d\boldsymbol{\tau}\, f_\kappa^e(\mathbf{u}) f_\kappa^{e*}(\boldsymbol{\tau})\exp[-W_\kappa(\mathbf{u}) \\
&\quad- W_\kappa(\boldsymbol{\tau})]\exp[2\pi i(\mathbf{b} - \mathbf{b}_\kappa)\cdot(\mathbf{u} - \boldsymbol{\tau})] \\
&\quad\times\{\exp[4\pi^2\langle(\mathbf{u}\cdot\mathbf{u}_\kappa)(\boldsymbol{\tau}\cdot\mathbf{u}_\kappa)\rangle] - 1\}
\end{aligned} \tag{43}$$

and

$$\begin{aligned}
&\langle\Delta V(\mathbf{b}', z')\Delta V(\mathbf{b}, z)\rangle \\
&\quad= \sum_\kappa\sum_{\kappa'}[\langle V_k(\mathbf{b}' - \mathbf{b}_\kappa, z')V_{\kappa'}(\mathbf{b} - \mathbf{b}_{\kappa'}, z)\rangle \\
&\qquad- V_{0k}(\mathbf{b}' - \mathbf{b}_\kappa, z')V_{0k'}(\mathbf{b} - \mathbf{b}_{\kappa'}, z)] \\
&\quad\simeq \sum_\kappa\sum_{\kappa'}\int d\mathbf{u}\int d\boldsymbol{\tau}\, f_\kappa^e(\mathbf{u}) f_{\kappa'}^e(\boldsymbol{\tau}) \\
&\qquad\times \exp[-W_\kappa(\mathbf{u}) - W_{\kappa'}(\boldsymbol{\tau})]\exp[2\pi i(\mathbf{b}' - \mathbf{b}_\kappa)\cdot\mathbf{u} \\
&\qquad- 2\pi i(\mathbf{b} - \mathbf{b}_{\kappa'})\cdot\boldsymbol{\tau}]\{\exp[4\pi^2\langle(\mathbf{u}\cdot\mathbf{u}_\kappa)(\boldsymbol{\tau}\cdot\mathbf{u}_{\kappa'})\rangle] - 1\},
\end{aligned} \tag{44}$$

where the sums of κ and κ' are limited to the atoms located in the crystal slices at depth z and z', respectively.

To prove the equivalence of the theory proposed here with that illustrated in §2.1, the first-order TDS approximation is made, so that $\exp(i\sigma' V) = \exp(i\sigma' V_0)\times \exp(i\sigma'\Delta V) \simeq \exp(i\sigma' V_0)[1 + i\sigma'\Delta V]$; thus,

$$\begin{aligned}
\langle\Gamma(\mathbf{b}', z')\Gamma^*(\mathbf{b}, z)\rangle &\simeq \sigma'^2\exp\{i\sigma'[V_0(\mathbf{b}', z') - V_0(\mathbf{b}, z)]\} \\
&\quad\times\langle\Delta V(\mathbf{b}', z')\Delta V(\mathbf{b}, z)\rangle.
\end{aligned} \tag{45}$$

If the phase-grating term $\exp\{i\sigma'[V_0(\mathbf{b}', z') - V_0(\mathbf{b}, z)]\}$ in (45) is ignored, (41) is thus approximated as

$$\begin{aligned}
I_{\mathrm{TDS}}(\mathbf{b}_p) &\simeq |4\pi^2\zeta|^2\sum_{n_c}\sum_{m_c}\int d\mathbf{b}\int d\mathbf{b}'\, D(\mathbf{b} - \mathbf{b}') \\
&\quad\times\langle\Delta U(\mathbf{b}', z_{n_c})\Delta U(\mathbf{b}, z_{m_c})\rangle\Phi_0(\mathbf{b}' - \mathbf{b}_p, z_{n_c}) \\
&\quad\times\Phi_0^*(\mathbf{b} - \mathbf{b}_p, z_{m_c}).
\end{aligned} \tag{46}$$

This equation is identical to (17).

The theory presented earlier by Wang & Cowley (1990) was based on the single-phonon scattering approximation, which retains only the $|\Delta V|^2$ term in (44). Under this approximation, (44) becomes

$$\langle[\Delta V(\mathbf{b}, z)]^2\rangle \simeq 4\pi^2\sum_\kappa\Big\langle\Big|\int d\mathbf{u}(\mathbf{u}\cdot\mathbf{u}_\kappa) f_\kappa^e(\mathbf{u})\exp[-W_\kappa(\mathbf{u})] \times\exp[2\pi i(\mathbf{b} - \mathbf{b}_\kappa)\cdot\mathbf{u}]\Big|^2\Big\rangle.$$

Thus, $\langle[\Delta V(\mathbf{b}, z)]^2\rangle = 0$ if $\mathbf{b} = \mathbf{b}_\kappa$, which means that the TDS generation function is zero at atomic core positions. This result is the consequence of the single-phonon scattering model. In numerical calculation, proper consideration of multiphonon processes [*i.e.* the higher-order terms in (44)] is important.

3. Imaging using diffusely scattered electrons in TEM

In HADF-TEM imaging (Bentley *et al.*, 1990), a plane wave is assumed to strike the crystal entrance face at an angle θ with respect to the optic axis (Fig. 5). The objective aperture is centered on the optic axis and allows the electrons scattered to a certain angular range to go through. The incident beam can be conically scanned around the optic axis in order to simulate the configuration of the ADF detector in STEM. The image obtained in this configuration is the average of the images obtained when the crystal is illuminated from different incident angles. Details regarding the image formation, experimental condition and dislocation contrast in HADF-TEM have been introduced previously (Wang, 1994). Here we mainly concentrated on the effects of dynamical diffraction on the image contrast.

The contribution of TDS electrons to the HADF-TEM image is

$$I_{\mathrm{TDS}}(\mathbf{b}) = \left\langle \left| \int \mathrm{d}\mathbf{b}'\, \delta\Phi_0(\mathbf{b}', d) T_{\mathrm{obj}}(\mathbf{b}' - \mathbf{b}) \right|^2 \right\rangle, \quad (47)$$

where $T_{\mathrm{obj}} = \mathbf{F}\{A(\mathbf{u}) \exp[i\pi(\lambda \Delta f u^2 + C_s \lambda u^4/2)]\}$ is the transfer function of the objective lens and objective aperture $A(\mathbf{u})$, Δf is the lens defocus and C_s is the lens spherical aberration coefficient. Substituting the wave function of the diffusely scattered electrons given by (10) into (47) results in

$$\begin{aligned} I_{\mathrm{TDS}}(\mathbf{b}) = |4\pi^2\zeta|^2 \Bigg\langle \Bigg| \sum_\kappa \Bigg\{ \int \mathrm{d}\mathbf{b}' \int_0^d \mathrm{d}z'\, T_{\mathrm{obj}}(\mathbf{b}' - \mathbf{b}) \\ \times O_p(\mathbf{b}', d - z')[\Delta U_\kappa(\mathbf{b}' - \mathbf{b}_\kappa, z' - z_\kappa, t) \\ \times \bar{\Phi}_0(\mathbf{b}', z')] \Bigg\} \Bigg|^2 \Bigg\rangle. \end{aligned} \quad (48)$$

If the dynamical diffraction effect of a single atom layer is neglected following the same argument as for (13) to (14), the integration of z' can be directly applied to ΔU_κ. Equation (48) is thus approximated as

$$\begin{aligned} I_{\mathrm{TDS}}(\mathbf{b}) &= |4\pi^2\zeta|^2 \Bigg\langle \Bigg| \sum_\kappa \{ \int \mathrm{d}\mathbf{b}' T_{\mathrm{obj}}(\mathbf{b}' - \mathbf{b}) \\ &\quad \times O_p(\mathbf{b}', d - z_\kappa)[\Delta U_\kappa(\mathbf{b}' - \mathbf{b}_\kappa, t) \\ &\quad \times \bar{\Phi}_0(\mathbf{b}', z_\kappa)] \} \Bigg|^2 \Bigg\rangle \\ &= |4\pi^2\zeta|^2 \sum_\kappa \sum_{\kappa'} \int \mathrm{d}\mathbf{b}' \int \mathrm{d}\mathbf{b}'' T_{\mathrm{obj}}(\mathbf{b}' - \mathbf{b}) T^*_{\mathrm{obj}}(\mathbf{b}'' - \mathbf{b}) \\ &\quad \times \langle \{ O_p(\mathbf{b}', d - z_\kappa)[\Delta U_\kappa(\mathbf{b}' - \mathbf{b}_\kappa, t) \bar{\Phi}_0(\mathbf{b}', z_\kappa)] \\ &\quad \times O^*_p(\mathbf{b}'', d - z_{\kappa'})[\Delta U_{\kappa'}(\mathbf{b}'' - \mathbf{b}_{\kappa'}, t) \bar{\Phi}^*_0(\mathbf{b}'', z_{\kappa'})] \} \rangle \\ &= |4\pi^2\zeta|^2 \sum_\kappa \sum_{\kappa'} \int \mathrm{d}\mathbf{b}' \int \mathrm{d}\mathbf{b}'' T_{\mathrm{obj}}(\mathbf{b}' - \mathbf{b}) T^*_{\mathrm{obj}}(\mathbf{b}'' - \mathbf{b}) \\ &\quad \times O_p(\mathbf{b}', d - z_\kappa) O^*_p(\mathbf{b}'', d - z_{\kappa'}) \{ \langle \Delta U_\kappa(\mathbf{b}' - \mathbf{b}_\kappa, t) \\ &\quad \times \Delta U_{\kappa'}(\mathbf{b}'' - \mathbf{b}_{\kappa'}, t) \rangle \bar{\Phi}_0(\mathbf{b}', z_\kappa) \bar{\Phi}^*_0(\mathbf{b}'', z_{\kappa'}) \}. \end{aligned} \quad (49)$$

The calculation of the HADF-TEM image is identical to that of HAADF-STEM if the transfer function $T_{\mathrm{obj}}(\mathbf{b}' - \mathbf{b}) T^*_{\mathrm{obj}}(\mathbf{b}'' - \mathbf{b})$ is replaced by the detector function $D(\mathbf{b}' - \mathbf{b}'')$. This is the result of the reciprocity theorem. Therefore, the discussions of cases *a–e* in §2.1.2 also apply to the TEM case. The approximation of ignoring the Bragg scattering after TDS (*i.e.* taking $O_p = 1$), however, does not hold in the TEM case owing to the small size of the objective aperture, thus the electron dynamical scattering out of the objective aperture becomes important. This is a key difference between HADF-TEM and HAADF-STEM.

The contribution of Bragg and Huang scattering electrons to the HADF-TEM image can be calculated by

$$I_{\mathrm{e}}(\mathbf{b}) = \left| \int \mathrm{d}\mathbf{b}'\, \Phi_0(\mathbf{b}', d) T_{\mathrm{obj}}(\mathbf{b}' - \mathbf{b}) \right|^2. \quad (50)$$

In the TEM case, the conical scan of the incident beam is equivalent to applying an average over the incident-beam direction in (49).

The theory presented in this section can also be applied to calculate the image formed by TDS electrons in high-resolution transmission electron microscopy because no restriction was made on the incident angle θ. Therefore, the theory covers all the practical experimental situations for both low- and high-angle diffuse scattering.

4. Diffraction and Huang scattering effects in HADF-TEM

4.1. *Contrast mechanism*

Diffuse scattering can be generated by both TDS and Huang scattering. TDS can be excited from wherever there are atoms, but Huang scattering can only be generated from the regions containing imperfections, such as defects or dislocations. For a perfect crystal, and if the image resolution is not sufficient to resolve lattice planes, the contribution made by TDS would be a background in the HADF-TEM image. In this case, contrast can be introduced due to Huang scattering from the regions containing defects or dislocations. This result has been observed experimentally and an image contrast mechanism has been proposed (Wang, 1994), as shown in Fig. 6. The dislocation contrast in HADF-TEM is generated by a two-step mechanism: the creation of diffuse scattering due to lattice distortion around the dislocation cores and the subsequent channeling propagation of the diffusely scattered electrons parallel or almost parallel to the optic axis, as governed by

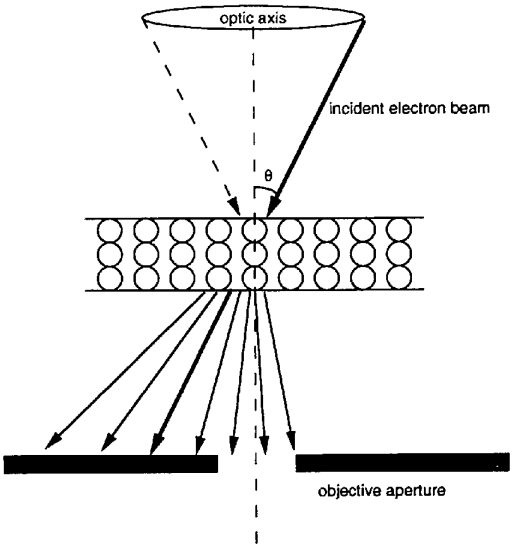

Fig. 5. Schematic diagram showing the formation of a *Z*-contrast image in TEM.

dynamical diffraction effects. The creation of local diffuse scattering is determined by the first step and the final image contrast is essentially determined by the second step. We now express the contrast mechanism into mathematical form.

Equation (49) can be modified to calculate the image formed by Huang scattering. For simplification, we assume that the spherical aberration coefficient $C_s = 0$, *i.e.* $T_{\text{obj}}(\mathbf{b}' - \mathbf{b}) = \delta(\mathbf{b}' - \mathbf{b})$. This is an excellent approximation for diffraction contrast imaging. Huang scattering is different from TDS in the way that the scattering from one atom site has no phase correlation with the scattering from the other atom sites. Based on (49), the image formed by Huang scattered electrons can be calculated by

$$I_H(\mathbf{b}) \simeq |4\pi^2\zeta|^2 \left| \int_0^d \mathrm{d}z\, O_p(\mathbf{b}, d-z) \Delta U(\mathbf{b}, z) \Phi_0(\mathbf{b}, z) \right|^2 \tag{51a}$$

with

$$\Delta U(\mathbf{r}) = \sum_\kappa \{U_\kappa[\mathbf{r} - \mathbf{r}_\kappa - \mathbf{R}(\mathbf{r})] - U_\kappa(\mathbf{r} - \mathbf{r}_\kappa)\}, \tag{51b}$$

where Φ_0 is the wave function of the incident electron, ΔU is the distorted crystal potential due to local lattice displacement $\mathbf{R}(\mathbf{r})$ introduced by defects; the product $[4\pi^2\zeta\Delta U\Phi_0]$ is the diffuse scattering generated at depth z; the subsequent dynamical scattering of the Huang scattered electrons is governed by the O_p operator (see §2.1.3). The integration on z sums over all the diffuse scattering generated in the entire crystal thickness. We now apply the Bloch-wave theory to perform the O_p calculation.

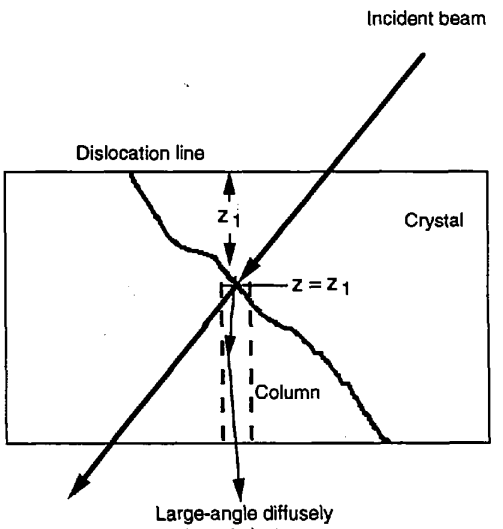

Fig. 6. Schematic diagram showing the contrast mechanism of HADF-TEM (see text). The dashed line indicates a column to be used for image calculation.

In HADF-TEM, since the angle between the incident electron beam and the optic axis of the microscope is large (> 50 mrad for 100 keV electrons), no strong dynamical scattering is expected if the beam direction is far from crystal zone axes so that the incident electron wave is assumed to be a plane wave when it strikes the defect, *i.e.* $\Psi_0(\mathbf{b}, z) \simeq \exp[2\pi i\mathbf{K}_b \cdot \mathbf{b} + 2\pi i K_z z]$, where $\mathbf{K}_b$ is the projection of the electron wave vector in the xy plane. After being diffusely scattered by the defect, the electrons that contribute to the HADF-TEM image are those propagating parallel or nearly parallel to the optic axis so that the column approximation can be made, as shown in Fig. 6. For each column, the diffuse scattering at the entrance of the column is $[4\pi^2\zeta\Delta U\Phi_0(\mathbf{b}, z)]$ and the wave in the column can be expressed in Bloch waves as

$$\Psi(\mathbf{K}, \mathbf{r}) = \sum_i \alpha_i(\mathbf{b}) \sum_g C_g^{(i)} \exp[2\pi i K_z z + 2\pi i \mathbf{g} \cdot \mathbf{b} + 2\pi i \nu_i (z - z_1)], \tag{52}$$

where z_1 is the depth of the defect region, ν_i is the eigenvalue of the Bloch wave i, and $\mathbf{g}$ is a reciprocal-space lattice vector. If the boundary condition $\Psi(\mathbf{K}, \mathbf{r}) = 4\pi^2\zeta\Delta U(\mathbf{b})\Psi_0(\mathbf{b}, z)$ is mached at the top of the column $z = z_1$, where $\Delta U(\mathbf{b}) = \int \mathrm{d}z\, \Delta U(\mathbf{b}, z)$ is the projected perturbation potential, the $\alpha_i(\mathbf{b})$ coefficient can be determined as

$$\alpha_i(\mathbf{b}) = 4\pi^2\zeta C_0^{(i)*} \Delta U(\mathbf{b}). \tag{53}$$

If the on-axis objective aperture selects only the $g = 0$ reflection, the intensity of the image is

$$I_H = \left| \sum_i \alpha_i(\mathbf{b}) C_0^{(i)} \exp[2\pi i \nu_i (d - z_1)] \right|^2 = |4\pi^2\zeta|^2 [\Delta U(\mathbf{b})]^2 \left| \sum_i C_0^{(i)*} C_0^{(i)} \exp[2\pi i \nu_i (d - z_1)] \right|^2. \tag{54}$$

To see the meaning of (54), the two-beam approximation is made. With the $C_0^{(i)}$ coefficients given by Hirsch, Howie, Nicholson, Pashley & Whelan (1977),

$$I_H = |4\pi^2\zeta|^2 [\Delta U(\mathbf{b})]^2 \{1 - \sin^2 \gamma_0 \sin^2[\pi \Delta\nu (d - z_1)]\}, \tag{55a}$$

where

$$\Delta\nu = \nu_1 - \nu_2 = [(KS_g)^2 + |U_g|^2]^{1/2}/K_z, \tag{55b}$$

$\gamma_0 = \arctan(KS_g/|U_g|)$, U_g is the Fourier coefficient of U and S_g is the excitation error. Equations (55) show that the contrast in the HADF-TEM image can be produced by four sources: (1) The spatial variation of ΔU owing to

different degrees of local lattice distortion. This effect is useful for the identification of dislocation cores. (2) The change of diffracting condition owing to the variation of crystal orientation as a result of crystal bending, for example, leading to the change of excitation error S_g (or γ_0). This effect has been observed in the following

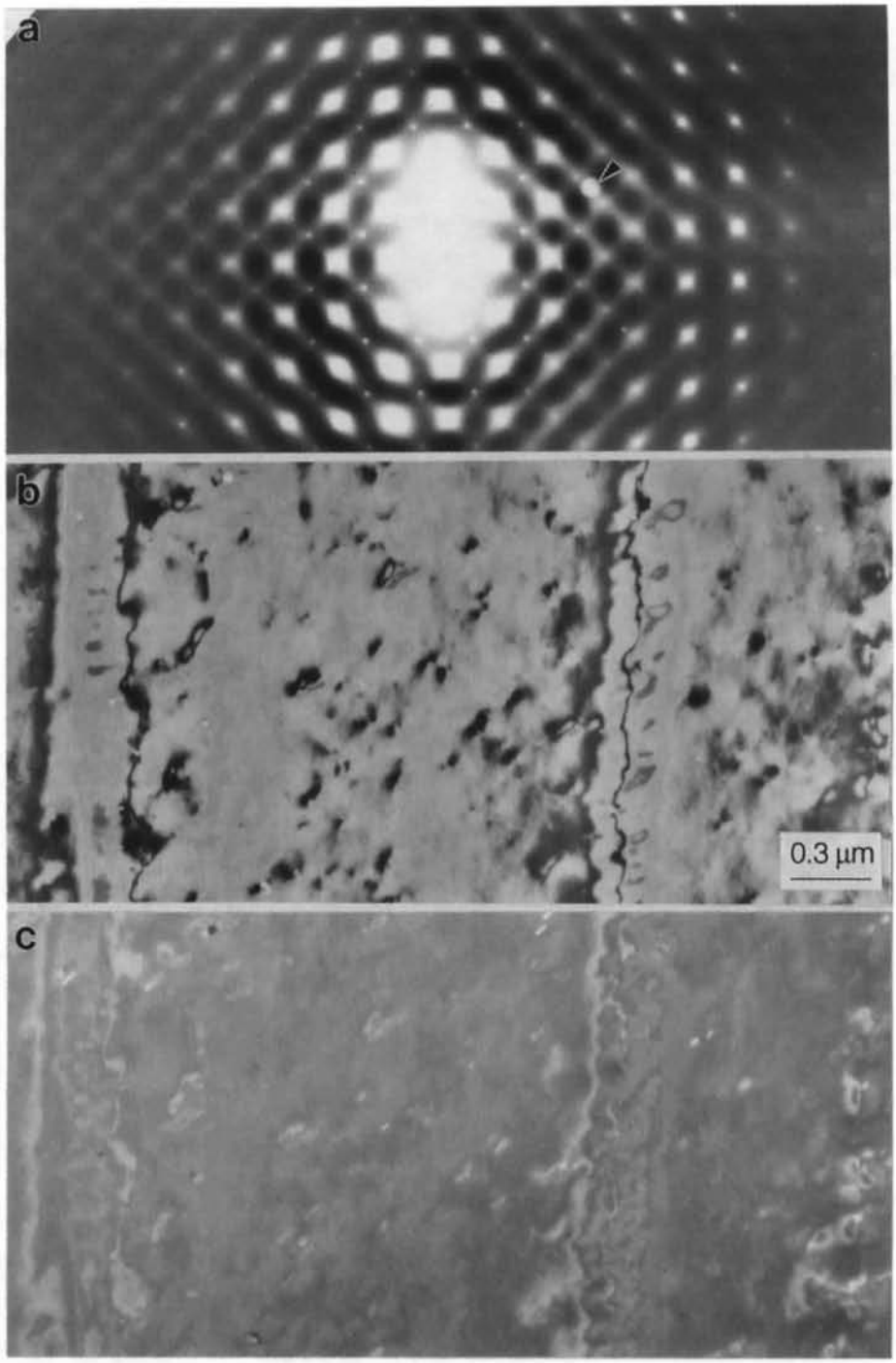

Fig. 7. Diffraction effect in dark-field imaging using diffusely scattered electrons: (*a*) is a double exposed electron diffraction pattern of a gold film, and (*b*) and (*c*) are the bright-field and dark-field images of the film, respectively. The arrowhead in (*a*) indicates the position and size of the objective aperture used to record the image in (*c*). Electron beam energy 300 keV.

experiments. (3) The depth z_1 of the dislocation can introduce some thickness-dependent effect, making it possible to identify the head and tail of a dislocation line (Wang, 1994). (4) The variation of the incident-beam direction introduces a slight change in K_z. This may also give some contrast according to (55*a*).

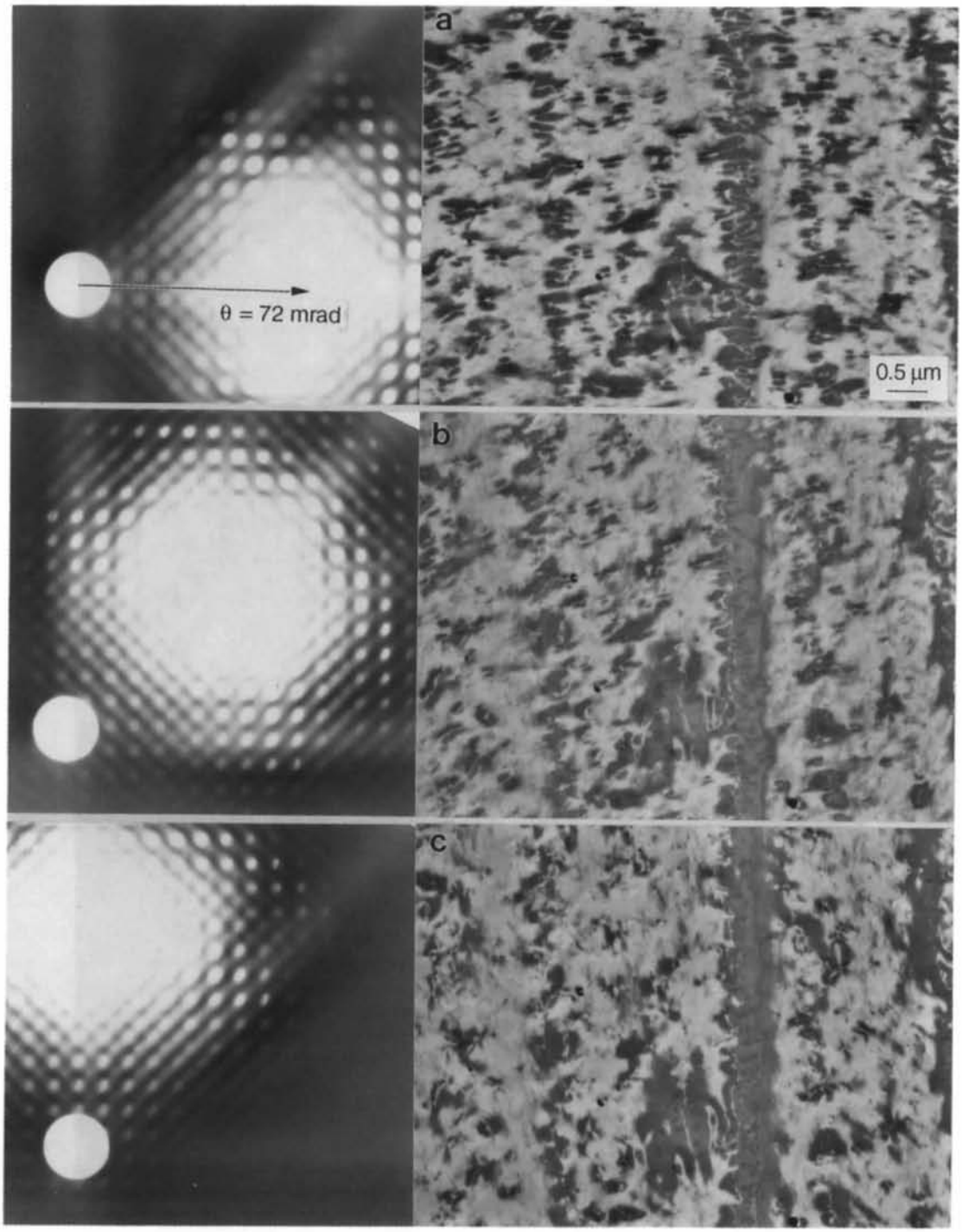

Fig. 8. Dark-field images of the gold film recorded at azimuth angles (*a*) $\varphi = 0$, (*b*) $\varphi = 45$ and (*c*) $\varphi = 90°$ and conical angle $\theta = 72$ mrad, showing the variation of image contrast with the change of incident-beam direction. The double exposed diffraction patterns for each case are shown on the left-hand side. Electron beam energy 300 keV.

For Bragg reflection, so that the excitation error $S_g = 0$, (55*a*) reduces to

$$I_H = \{|4\pi^2\zeta|^2[\Delta U(\mathbf{b})]^2\}\cos^2[\pi\Delta\nu(d - z_1)]. \quad (56)$$

This equation has the same form as that for conventional on-axis bright-field diffraction contrast imaging (Hirsch *et al.*, 1977):

$$I_0 = \cos^2(\pi d\Delta\nu). \quad (57)$$

Therefore, the HADF-TEM shares many characteristics with the conventional diffraction contrast imaging. The thickness dependence of the two types of images may be different, however.

4.2. *Experimental observations*

Dynamical diffraction effects are easily seen in the HADF-TEM because of its flexibility of controlling the diffracting condition so that only the diffusely scattered electrons are selected to form the image. Fig. 7(*a*) shows a double exposed electron diffraction pattern of a single-crystalline gold foil oriented near the [100] zone axis. Fig. 7(*b*) is a bright-field image of the foil and Fig. 7(*c*) is the corresponding dark-field image recorded using the diffusely scattered electrons as indicated by an arrowhead in Fig. 7(*a*). In the diffraction pattern, ⟨100⟩ streaks produced by TDS are clearly seen. The bright-field image shows some bending and strain contrast. Most of the features observed in the bright-field image are shown

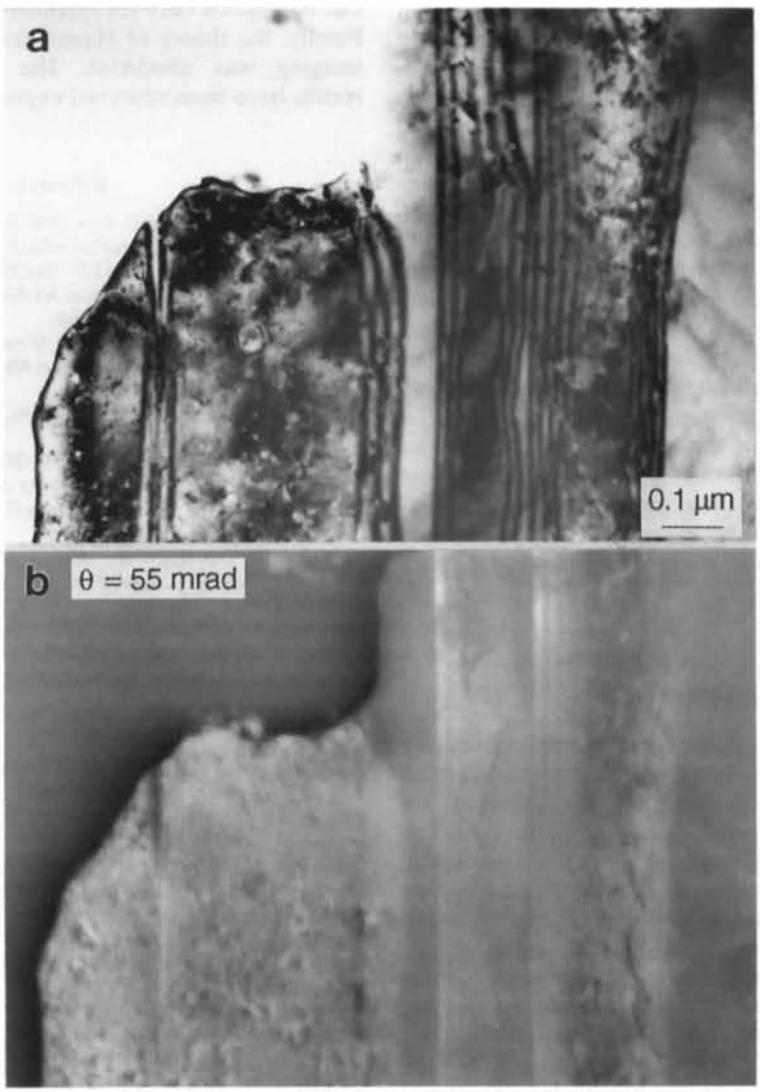

Fig. 9. (*a*) Bright-field and (*b*) conical-scan HADF-TEM images of a silver film, showing the interference fringes at the inclined {111} twin boundaries. Conical angle $\theta = 72$ mrad, electron beam energy 300 keV.

in the dark-field image of the diffusely scattered electrons. The contrast in Figs. 7(*b*) and (*c*) is reversed and the figures appear to be complementary in contrast. This observation clearly shows the importance of the diffraction effect in the imaging of diffusely scattered electrons, and it also shows the similarity of HADF-TEM with a conventional bright-field diffraction contrast image, as expected theoretically according to (56) and (57).

To further check the diffraction effect in HADF-TEM, the gold foil was tilted to the [100] zone axis so that the objective aperture is placed exactly on the [100] pole. Fig. 8 shows dark-field images of the gold foil recorded when the incident beam was stopped at three azimuth positions. The double exposed diffraction pattern for each image is shown on the left-hand side. It is apparent that the three images have different contrast distributions due to slight variation of diffracting condition (or S_g). This observation again shows the diffraction effect in HADF-TEM imaging, in agreement with the theoretically expected result (55*a*). In practice, if the image is recorded under continuous conical scan, the observed image contrast is an average of the contrast for each scan position.

Fig. 9 shows bright-field and conical scan HADF-TEM images of a silver foil that contains inclined {111} twin boundaries. The interference fringes of the twin boundaries are observed not only in the bright-field image but also in the conical-scan HADF-TEM image. The fringe contrast is complementary in both images. This observation agrees with the prediction of the theory illustrated in the last section.

The experimental data shown in this section demonstrate clearly the vital effect of dynamical diffraction in atomic number sensitive imaging using diffusely scattered electrons. It is thus necessary to include this effect in the image calculation following the dynamical theories proposed in §§2 and 3.

5. Concluding remarks

In this paper, 'exact' dynamical theories of atomic number sensitive images (or Z-contrast images) formed by thermal diffusely scattered (TDS) electrons are proposed based on first-principles considerations. The theories are derived for simulating the images obtained either in scanning transmission electron microscopy (STEM) using an annular dark-field detector or in transmission electron microscopy (TEM) using an on-axis objective aperture under hollow-cone beam illumination. No approximation was made in treating the thermal vibration of the crystal atoms. The time average of the signal intensities contributed by the thermal diffuse scattering of various instantaneous crystal lattice configurations has been performed before numerical calculation. The following effects are comprehensively covered in the theory: dynamical diffraction of the beam before and after TDS, thickness-dependent beam broadening or channeling, Huang scattering from defect regions, coherence of the thermal diffusely scattered electrons generated from the atomic layers packed within the coherent length, multiphonon and multiple phonon excitations, and the detection geometry. The theory is formulated in the multislice scheme that is best suited for practical numerical calculations, especially when defects and interfaces are involved. The coherent length in the z direction varies with the change of atomic mass in the column. It is thus possible that the z coherence may disappear for heavy elements.

Other simplified theories have been derived from this unified theory under various approximations. It has been shown that the incoherent imaging theory is a very simplified case of the practical imaging condition and it can be applied only for qualitative image interpretation. Finally, the theory of Huang scattering in HADF-TEM imaging was illustrated. The theoretically expected results have been observed experimentally.

References

AMALI, A. & REZ, P. (1992). *Proc. 50th Annual Meeting of the Electron Microscopy Society of America*, edited by G. W. BAILEY, J. BENTLEY & J. A. SMALL, pp. 1226–1227. San Francisco Press.

ARFKEN, G. (1970). *Mathematical Methods for Physicists*, 2nd ed., p. 485. New York: Academic Press.

BENTLEY, J., ALEXANDER, K. B. & WANG, Z. L. (1990). *Proc. XIIth International Congress for Electron Microscopy (Seattle)*, Vol. 2, pp. 400–401. San Francisco Press.

BLELOCH, A. L., CASTELL, M. R., HOWIE, A. & WALSH, C. A. (1994). *Ultramicroscopy*, **54**, 107–115.

BORN, M. (1942). *Rep. Prog. Phys.* **9**, 294–333.

BRÜESCH, P. (1982). *Phonons: Theory and Experiments* I – *Lattice Dynamics and Models of Interatomic Forces*. Berlin/Heidelberg/New York: Springer-Verlag.

COENE, W. & VAN DYCK, D. (1990). *Ultramicroscopy*, **33**, 261–267.

COWLEY, J. M. (1969). *Appl. Phys. Lett.* **15**, 58–59.

COWLEY, J. M. (1988). *Acta Cryst.* A**44**, 847–855.

COWLEY, J. M. & HUANG, Y. (1992). *Ultramicroscopy*, **40**, 171–180.

COWLEY, J. M. & MOODIE, A. F. (1957). *Acta Cryst.* **10**, 609–619.

EAGLESHAM, D. J. & BERGER, S. D. (1994). *Ultramicroscopy*, **53**, 319–324.

FANIDIS, C., VAN DYCK, D., COENE, W. & VAN LANDUYT, J. (1989). *Computer Simulation of Electron Microscope Diffraction and Images*, edited by W. KRAKOW & M. O'KEEFE, pp. 135–137. Washington, DC. The Minerals, Metals and Materials Society.

FANIDIS, C., VAN DYCK, D. & VAN LANDUYT, J. (1992). *Ultramicroscopy*, **41**, 55–64.

GOODMAN, P. & MOODIE, A. F. (1974). *Acta Cryst.* A**30**, 280–290.

HALL, C. R. (1965). *Philos. Mag.* **12**, 815–826.

HALL, C. R. & HIRSCH, P. B. (1965). *Proc. R. Soc. London Ser. A*, **286**, 158–177.

HILLYARD, S., LOANE, R. F. & SILCOX, J. (1993). *Ultramicroscopy*, **49**, 14–25.

HILLYARD, S. & SILCOX, J. (1993). *Proc. 51st Annual Meeting of the Electron Microscopy Society of America*, edited by G. W. BAILEY & C. L. RIEDER, pp. 976–977. San Francisco Press.

HIRSCH, P. B., HOWIE, A., NICHOLSON, R. B., PASHLEY, D. W. & WHELAN, M. J. (1977). *Electron Microscopy of Thin Crystals*. Huntington, New York: Krieger.

ISHIZUKA, K. (1982). *Acta Cryst.* A**38**, 773–779.

JESSON, D. E. & PENNYCOOK, S. J. (1993). *Proc. 51st Annual Meeting of the Electron Microscopy Society of America*, edited by G. W. BAILEY & C. L. RIEDER, pp. 978–979. San Francisco Press.
KONNERT, J. & D'ANTONIO, P. (1991). *Ultramicroscopy*, **38**, 169–179.
LIU, J. & COWLEY, J. M. (1991). *Ultramicroscopy*, **37**, 50–71.
OTTEN, M. T. (1991). *J. Electron Microsc. Tech.* **17**, 221–230.
PENNYCOOK, S. J. & JESSON, D. E. (1990). *Phys. Rev. Lett.* **64**, 938–941.
PENNYCOOK, S. J. & JESSON, D. E. (1991). *Ultramicroscopy*, **37**, 14–38.
PEROVIC, D. D., HOWIE, A. & ROSSOUW, C. J. (1993). *Philos. Mag. Lett.* **67**, 261–272.
SPENCE, J. C. H., ZUO, J. M. & LYNCH, J. (1989). *Ultramicroscopy*, **31**, 233–240.
TAKAGI, S. (1958). *J. Phys. Soc. Jpn*, **13**, 278–286.
TREACY, M. M. J. (1993). *Proc. 51st Annual Meeting of the Electron Microscopy Society of America*, edited by G. W. BAILEY & C. L. RIEDER, pp. 748–749. San Francisco Press.
TREACY, M. M. J. & GIBSON, J. M. (1993). *Ultramicroscopy*, **52**, 31–53.
VAN DYCK, D. (1975). *Phys. Status Solidi B*, **72**, 321–331.
VAN DYCK, D. (1983). *J. Microsc. (Oxford)*, **132**, 31–42.
VAN DYCK, D. (1985). *Adv. Electron. Electron Phys.* **65**, 295–355.
WANG, Z. L. (1992). *Philos. Mag.* **B65**, 559–587.
WANG, Z. L. (1994). *Ultramicroscopy*, **53**, 73–90.
WANG, Z. L. (1995). *Elastic and Inelastic Scattering in Electron Diffraction and Imaging*. New York: Plenum Press.
WANG, Z. L. & BENTLEY, J. (1991). *Ultramicroscopy*, **38**, 181–213.
WANG, Z. L. & COWLEY, J. M. (1989). *Ultramicroscopy*, **31**, 437–453.
WANG, Z. L. & COWLEY, J. M. (1990). *Ultramicroscopy*, **32**, 275–289.
WANG, Z. L. & LI, D. C. (1995). *Philos. Mag.* **B71**, 201–219.
WARREN, B. E. (1990). *X-ray Diffraction*, ch. 11. New York: Dover.
XU, P., KIRKLAND, E. J., SILCOX, J. & KEYSE, R. (1990). *Ultramicroscopy*, **32**, 93–102.
YOSHIOKA, H. (1957). *J. Phys. Soc. Jpn*, **12**, 618–628.